Review

Radio Frequency Coils for Hyperpolarized [13]C Magnetic Resonance Experiments with a 3T MR Clinical Scanner: Experience from a Cardiovascular Lab

Giulio Giovannetti [1,*], Alessandra Flori [2], Maria Filomena Santarelli [1], Vincenzo Positano [2], Nicola Martini [2], Roberto Francischello [2], Rolf F. Schulte [3], Jan Henrik Ardenkjaer-Larsen [4], Luca Menichetti [1], Giovanni Donato Aquaro [2], Andrea Barison [2] and Francesca Frijia [2]

[1] Institute of Clinical Physiology, National Research Council (CNR), 56124 Pisa, Italy; santarel@ifc.cnr.it (M.F.S.); luca.m@ifc.cnr.it (L.M.)
[2] Fondazione CNR/Regione Toscana G. Monasterio, 56124 Pisa, Italy; alessandra.flori@ftgm.it (A.F.); positano@ftgm.it (V.P.); nicola.martini@ftgm.it (N.M.); roberto.francischello@gmail.com (R.F.); aquaro@ftgm.it (G.D.A.); dr.andrea.barison@gmail.com (A.B.); f.frijia@ftgm.it (F.F.)
[3] GE Healthcare, Freisinger Landsrt., 50 85748 Garching, Germany; schulte@ge.com
[4] Health Technology, Danish Technical University, 2800 Kongens Lyngby, Denmark; jhar@dtu.dk
[*] Correspondence: giovannetti@ifc.cnr.it

Abstract: Hyperpolarized 13C magnetic resonance (MR) is a promising technique for the noninvasive assessment of the regional cardiac metabolism since it permits heart physiology studies in pig and mouse models. The main objective of the present study is to resume the work carried out at our electromagnetic laboratory in the field of radio frequency (RF) coil design, building, and testing. In this paper, first, we review the principles of RF coils, coil performance parameters, and estimation methods by using simulations, workbench, and MR imaging experiments. Then, we describe the simulation, design, and testing of different 13C coil configurations and acquisition settings for hyperpolarized studies on pig and mouse heart with a clinical 3T MRI scanner. The coil simulation is performed by developing a signal-to-noise ratio (SNR) model in terms of coil resistance, sample-induced resistance, and magnetic field pattern. Coil resistance was calculated from Ohm's law and sample-induced resistances were estimated with a finite-difference time-domain (FDTD) algorithm. In contrast, the magnetic field per unit current was calculated by magnetostatic theory and a FDTD algorithm. The information could be of interest to graduate students and researchers working on the design and development of an MR coil to be used in 13C studies.

Keywords: magnetic resonance; radio frequency coils; simulation

1. Introduction

Cardiovascular magnetic resonance (CMR) represents a powerful tool in the noninvasive assessment of cardiac anatomy, function, and metabolism [1]. CMR applications cover a broad spectrum of clinical and research areas, such as global and regional cardiac function, myocardial perfusion, myocardial viability, tissue characterization, and proximal coronary anatomy.

Magnetic resonance spectroscopy (MRS) represents an accurate, noninvasive, nonionizing tool for in vivo evaluation of cardiac metabolism, with applications to various nuclei (^{1}H, ^{31}P, ^{13}C) [2,3].

In particular, 13C spectroscopy can be used for an investigation of the intermediary metabolism of biomolecules in vivo [4]. [13]C nuclei generate a natural signal, which is very low and difficult to detect with conventional magnetic resonance (MR) scanners due to

the scarce natural abundance and the low level of nuclear polarization at thermal equilibrium. The low ^{13}C signal is even more critical if the study involves a moving organ such as the heart. Recently, the development of hyperpolarization techniques for enhancing ^{13}C polarization has led to a significant nuclear magnetization increase. In particular, the hyperpolarization technology known as dissolution dynamic nuclear polarization (dDNP) enhances the polarization of ^{13}C by a factor of 100,000 [5].

However, several technological problems still limit the application of these techniques and require innovative solutions, especially when a low molar concentration of metabolites reduces the in vivo sensitivity.

Despite the use of hyperpolarized ^{13}C tracers, the design and development of both dedicated radio frequency (RF) coils and acquisition settings need to be specialized for the region of interest, and potentially for the animal of interest, to provide the optimal signal-to-noise ratio (SNR). In particular, RF coils have to guarantee a large field of view (FOV) with high magnetic field homogeneity in transmission (TX) and to achieve high SNR in reception (RX) [6]. Moreover, ^{13}C experiments require that the MR system operates at two different frequencies (multinuclear system) to provide 1H imaging and ^{13}C acquisition with the same experimental setup. Multinuclear acquisitions can be performed by using two separate RF coils or by using a single dual-tuned coil operating at two different frequencies. The choice of the most suitable coil for a given application is a necessary constraint. Recently, a quality assurance imaging protocol for ^{13}C coils based on MR spectroscopic imaging was described in the literature [7], in which different coil setups were tested and compared.

After a brief introduction to hyperpolarization techniques and hyperpolarized ^{13}C MR applications, then, we review the RF coil principles, the coil performance parameters, and their estimation methods, starting from simulations and workbench tests to MR experiments. In the second part of this paper, we summarize the design of a coil and the results obtained in phantom tests and in vivo studies with a clinical 3T MRI scanner located in our cardiovascular lab.

Sin this paper, we have summarized both the theory and our experience with ^{13}C coil design and evaluation, and therefore, the information should be of interest to graduate students and researchers in the field of MR coil design and development, especially for ^{13}C studies.

2. Hyperpolarized 13C Magnetic Resonance

Hyperpolarization increases the measured MR signal strength by many orders of magnitude, thus, overcoming the intrinsic MR sensitivity limitations [8].

Hyperpolarized ^{13}C has been investigated for imaging the metabolism in various cancers and cardiac diseases. The most common hyperpolarized ^{13}C-labeled agents include small molecules that play a central role in the major metabolic cycles in normal and diseased functions. In particular, [1-^{13}C]pyruvate is rapidly transported to the intracellular space via the monocarboxylate transporters, where it is used as a probe to track the intracellular metabolism. [1-^{13}C]pyruvate has been applied to investigate metabolic disorders, tumor response to therapy, cancer detection, cerebral dynamics and metabolism, pH, and more.

In addition to pyruvate, other hyperpolarized ^{13}C substrates have been investigated from [1,4-[13]C_2]fumarate to [1,4-[13]C_2]malate. Moreover, ^{13}C-bicarbonate and ^{13}C-carbon dioxide have been investigated to measure extracellular pH. Other ^{13}C-labeled substrates applied to cardiac functional or metabolic imaging include [U-^{13}C]α-ketobutyrate, [1-^{13}C]lactic acid, [1-^{13}C]acetate, ^{13}C-urea, and [1-^{13}C]butyrate [9].

The most common ^{13}C-labeled agents include small molecules that play a central role in the major metabolic cycles in normal and diseased functions. For a given metabolic pathway, the choice of metabolic substrate and the specific ^{13}C label site dictate the T1 time and the metabolic tracer's chemical shift. In turn, the T1 time influences the total acquisition time and SNR for imaging and spectroscopy. The chemical shift may further

constrain acquisition parameters (e.g., echo time or RF excitation bandwidth) depending on the spectral bandwidth required to discriminate between different metabolic species.

Among the hyperpolarization techniques, currently, dDNP is the most promising from a clinical perspective [5,10]. In brief, dDNP is performed at high magnetic field (3.35 to 7 T) and extremely low temperature (≈1 K), where the high polarization of electron spins (unpaired electrons of radical molecules added to the sample at mM concentration) is transferred to nuclear spins by microwave irradiation. Rapid dissolution of the sample is subsequently performed to produce hyperpolarized solutions that can be injected for in vivo studies [11]. The ^{13}C-pyruvate is the gold-standard molecule for DNP clinical and preclinical applications due to its optimal chemo-physical properties, long T1 relaxation time, high ^{13}C concentration, as well as its key role in cell metabolism. To investigate tissue metabolism, an isotopically labeled compound (usually a ^{13}C-enriched molecule such as ^{13}C-pyruvate) is hyperpolarized and readily injected in vivo, where it participates in enzyme-mediated metabolic reactions. Using MRS, the injected compound and its metabolic products can be selectively detected in a noninvasive manner and in real time [12,13].

The hyperpolarized signal rapidly decays once the hyperpolarization process is concluded due to T1 relaxation. For the most used ^{13}C-labeled compounds, T1 is of the order of a few tens of seconds, and the MR signal decay occurs in a few minutes. Because of this rapid and irreversible decay, fast signal detection with high SNR, as well as efficient use of the magnetization, are needed for in vivo hyperpolarization studies.

3. RF Coil Theory and Design

The study of metabolism with hyperpolarized tracers requires a dedicated technical setup. For example, the experiments would benefit from the improvement of gradient performance and the use of ultra-high field (UHF) scanners (7T or above) since the SNR is linearly proportional to field strength [14]. Nevertheless, RF dedicated coils are an essential component in these experiments to fully exploit the MR signal enhancement.

3.1. RF Coil as RLC Circuit

RF coils are designed so that the flowing current is maximal at the Larmor frequency ($f_0 = \gamma/2\pi \, B_0$, where B_0 is the static field and γ is the gyromagnetic ratio with 42.58 MHz/T and 10.71 MHz/T values for 1H and ^{13}C nuclei, respectively) which corresponds to the coil resonant frequency. The bandwidth of the coil resonance has to be large enough to cover the various chemical resonances, i.e., about 30 ppm for hyperpolarized [1-^{13}C]pyruvate (to detect the main metabolites [1-^{13}C]lactate, [1-^{13}C]alanine, and [1-^{13}C]bicarbonate) [8,13].

The coil can be schematized with an equivalent RLC circuit (Figure 1), where *L* represents the system inductance, which takes into account the energy stored in the magnetic field, and *C* is the system capacitance mainly resulting from the discrete capacitors contribution. The coil resonant frequency corresponds to the frequency for which the current assumes the maximum value:

$$f_0 = \frac{1}{2\pi\sqrt{LC}} \tag{1}$$

The term *R* is the sum of all the resistances that can be associated with loss mechanisms within the conductors and within the sample [6]. In particular,

$$R_{tot} = R_{coil} + R_{sample} + R_{extra}. \tag{2}$$

Rcoil, which depends on the conductor geometry, takes into account the conductor losses; *Rsample* represents the sample losses caused by RF currents, induced by electric fields in the sample and fluctuating magnetic field and, mainly generated by the coil capacitors; and *Rextra* includes radiative and tuning capacitors losses, which can be neglected in many applications.

3.2. Coil Inductance Calculation

The inductance of conductor portions can be calculated by using the following expression [15]:

$$L = \frac{\mu_0}{4\pi I^2} \iiint_V \iiint_V \frac{J(r) \cdot J(r')}{R} \, dv \, dv' \tag{3}$$

where J represents the current density in the conductor, μ_0 is the permeability of free space, I is the total current in the conductor, V is the conductor volume, and $R = |r - r'|$, see Figure 1.
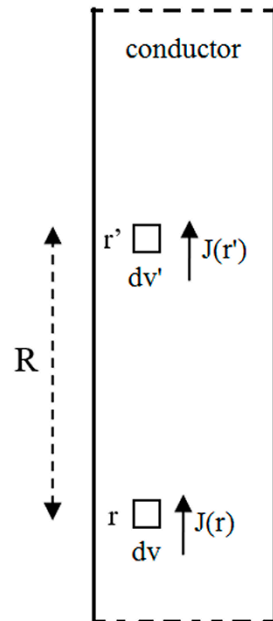

Figure 1. Inductance calculation according to Equation (3).

Conductors used for building RF coils can be divided into the following two groups, depending on their cross-sectional shape: wires (cylindrical rod shapes, defined by their radius) and strips (rectangular shapes, characterized by width and thickness). A simple relationship between strip and wire conductors' sizes is used to evaluate the equivalent width (w) of a wire of radius a, while maintaining the same inductance value as w = 4.482 a [15].

3.3. Coil Performance Parameters Definition

A quantitative measure of circuit quality is provided by the definition of the coil quality factor (Q) [15] as follows:

$$Q = 2\pi \frac{\text{energy stored in i -th cycle}}{\text{energy dissipated during in-th cycle}} \tag{4}$$

Which can be expressed in terms of circuit parameters as:

$$Q = \frac{2\pi f_0 L}{R_{tot}} = \frac{1}{R_{tot}} \sqrt{\frac{L}{C}} \tag{5}$$

Coil performance evaluation can also be described with the ratio r between the quality factor of the empty resonator ($Q_{unloaded}$) and the resonator in the presence of the sample (Q_{loaded}):

$$r = \frac{Q_{unloaded}}{Q_{loaded}} = 1 + \frac{R_{sample}}{R_{coil} + R_{extra}} \tag{6}$$

The maximal SNR can be achieved when r is maximized [16].

Another parameter describing the coil performance both in transmission and in reception mode is efficiency, defined as the ratio between the intensity of the magnetic field B_1 at a given point in space and the corresponding power P [6]:

$$\eta = \frac{B_1}{\sqrt{P}} \tag{7}$$

3.4. Signal-to-Noise Ratio (SNR) Estimation

The SNR of the acquired MR signals strongly affects the quality of the reconstructed data; therefore, the RF coils have to be designed to provide the higher *SNR*. The theoretical *SNR* can be calculated as the ratio between the induced radio frequency signal and the root mean square (RMS) of the thermal noise voltage measured at the coil terminals [17]:

$$SNR_P = \frac{2\pi f_0 M V B_P}{\sqrt{4kT\Delta f R_{tot}}} \tag{8}$$

where f_0 is the Larmor frequency; M is the magnetization; V is the voxel volume; B_P is the receiver coil magnetic field per unit current at the observation point P; k is the Boltzmann constant; T is the absolute resistance temperature; Δf is the receiver bandwidth; and R_{tot} is the total noise resistance, calculated as described in Equation (2).

Therefore, for the SNR evaluation, it is necessary to calculate the magnetic field B_P and the different losses contributions.

3.4.1. Magnetic Field: Magnetostatic Method

The magnetostatic theory is based on the nearly static field assumption, which holds only when the coil dimensions are much lower than the wavelength. The static magnetic field produced by a steady electric current, I, flowing in an arbitrary closed contour, C, can be calculated by using Biot–Savart law [15] as:

$$B(r) = \frac{\mu_0 I}{4\pi} \int_C \frac{dl \wedge R}{R^3} \tag{9}$$

where $\mu_0 = 4\pi \times 10^{-7}$ (H/m) is the free space permeability, dl is the infinitesimal vector tangential to C, and R is the distance between the conductor path and the observation point.

The Biot–Savart equation can be used for the coils three-dimensional B_1 field distributions evaluation.

The magnetic field calculation generated by the currents along the coil conductors can be performed by subdividing the coil path into segments to study their total magnetic field contribution separately. The conductor sizes can be neglected with respect to the wavelength, and the magnetic field generated by the currents can be evaluated considering conductors as very thin wires.

3.4.2. Magnetic Field: Finite-Difference Time-Domain (FDTD) Method

Some coil characteristics, such as field homogeneity, can be estimated using electromagnetic theory such as Biot–Savart law, as long as the nearly static field assumption holds, but with the increase in Larmor frequency in current scanners, this condition is not always satisfied. Moreover, when the coil is loaded with a sample, the SNR distribution is affected by its electromagnetic properties, and only numerical methods simulate the coil behavior in loaded condition to design coils with a complex shape. In general, numerical methods estimate the magnetic field of the RF coil when loaded with a model of the exposed body, by providing a numerical solution of Maxwell's equations with specific

boundary conditions. Such methods can be classified according to whether the computation is made in the time or frequency domain, and if the method is based on differential or integral equations. For our research [18], we employed the finite-difference time-domain (FDTD) method [19], which incorporated complex structures into the computational space, such as part of the human body for studying the electromagnetic interaction between the coil and the biological phantom. Many studies have confirmed that FDTD is a useful tool for evaluating and optimizing the RF coil design. For example, Amjad [20] performed the power deposition calculation inside a phantom for an RF-induced temperature rise, while Chen [21] evaluated the specific absorption rate (SAR) and B_1 field pattern inside a human head for a shielded birdcage coil. Wang [22] described SAR and temperature calculation in a volume coil loaded with a human head at different frequencies. In [23], the FDTD method was used for comparing B_1 homogeneity between a 16-leg high-pass birdcage coil and an eight-channel phased-array coil loaded with water phantom and head model, both designed for 3T MRI, by exploiting the FDTD possibility to estimate the B_1 value for each point inside the sample. The simulation results evidenced that the standing wave effect heavily affected birdcage coil field homogeneity, while the phased-array coil showed better performance. The ability of FDTD for estimating RF coils inductance was described in [24] with an example of a square loop constituted by a different diameter wire conductor, whose FDTD calculation was compared with an analytical value, providing a difference within 3%, while the addition of discrete capacitors permitted the coil to resonate at the desired frequency. The FDTD can even be used for predicting electromagnetic interference between wireless devices, as described in [25], where an FDTD-based commercial tool was employed for accurately calculating the interference voltage induced at the connector of an implantable cardiac pacemaker placed inside a human torso phantom, due to the electromagnetic fields generated around wireless power transmission (WPT) antennas.

3.4.3. Coil Losses

The coil resistance can be estimated by accounting for the conducting pathway geometry and by using the following classic formula:

$$R_{coil} = \frac{\rho L}{S} \tag{10}$$

where ρ is the conductor resistivity, and L and S are the total conductor length and cross-sectional area, respectively [26]. S is limited by the value of the penetration depth δ [27] as follows:

$$\delta = \sqrt{\frac{\rho}{\pi f \mu_o}} \tag{11}$$

where ρ is the conductor resistivity ($\rho = 1.68 \cdot \times 10^{-8}$ $\Omega \cdot$m for copper) and f is the coil tuning frequency.

While a wire conductor is characterized by a uniform current distribution inside its cross-sectional area defined by penetration depth (classical skin effect), for a strip conductor, the current density has the tendency of concentrating at conductor edges (lateral skin effect) [28] and increases the conductor resistance, becoming the dominant mechanism at high frequencies [29].

3.4.4. Sample-Induced Losses

Sample-induced resistance calculation was performed by using commercial tools based on the FDTD method and by developing an algorithm based on the theory of the resonant circuit [30].

After perturbing the resonant circuit with a Gaussian pulse and observing the voltage oscillation damping, the system Q factor can be calculated as described in Equation (4)

and by taking into account that the energy stored by a capacitor is proportional to the square of the voltage across its layers as:

$$Q = 2\pi \frac{V_i^2}{V_i^2 - V_{i+1}^2} \qquad (12)$$

where V_i and V_{i+1} are the voltage values at ith and $(i + 1)$th cycles, respectively.

By performing a system simulation with the coil conductor consisting of a perfect electric conductor (PEC), the coil resistance vanishes completely, and Equation (5) can be used to estimate the series resistance value taking into account the energy dissipated in the system as follows:

$$R_S = \frac{2\pi f_0 L}{Q} \qquad (13)$$

where f_0 represents the coil resonant frequency, and L represents the coil inductance value.

3.5. Coil Classification: Surface, Volume, and Phased-Array Coils

The coils used in MR can be categorized into volume and surface coils, according to their geometries [31]. Volume coils are often used for both transmission and reception, since they can generate a homogeneous magnetic field in a large region surrounding the sample. The most common configuration for a volume coil is the birdcage, constituted by n legs connected at each end to two circular loops (end rings) [32], which can generate a highly homogeneous field with a high SNR. The surface coil configurations include loop coils of various shapes, which are much smaller than the volume coils and provide higher SNR in the coil proximity. In general, they are mainly used as receiver coils due to the relatively low field homogeneity, even if transmit coil or transceiver surface coil applications have been reported. Phased-array coils [33] provide a large region of sensitivity, similar to that achieved with volume coils, and a high SNR, usually associated with surface coils. All elements of the array are separately connected to receiver channels whose outputs are optimally combined with a phase correction, which is dependent on the point in space from which the signal originates. Figure 2 shows an example of SNR images obtained with different geometrical coils for the same cylindrical phantom [7]. Volume (birdcage and Helmholtz), phased array (8, 14, and 16 channels), and surface coils provide very different SNR distributions.
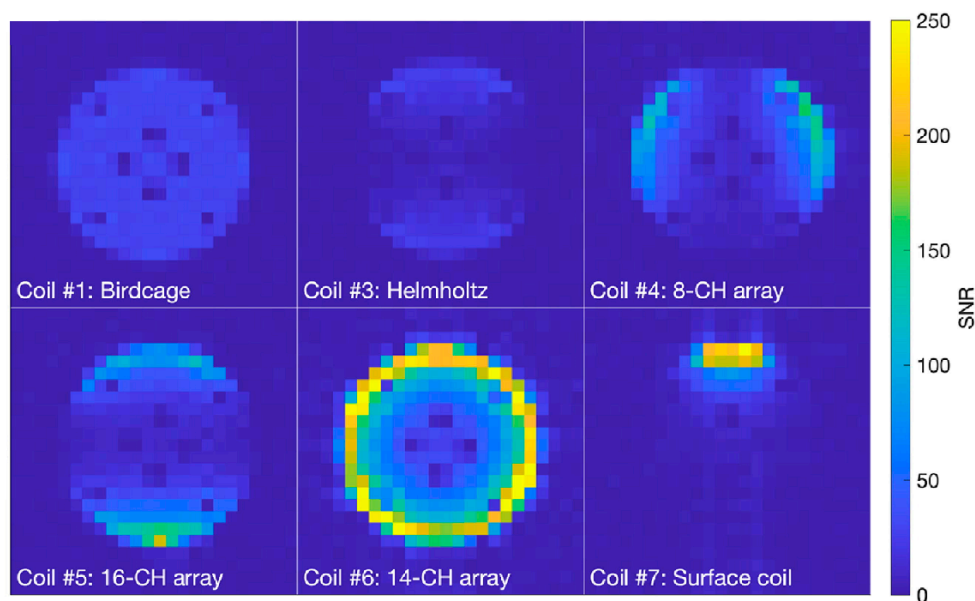

Figure 2. Signal-to-noise ratio (SNR) images obtained with different geometry coils. Reprinted from the *Journal of Magnetic Resonance* 2020 [7].

3.6. Coil Performance Parameters Workbench Estimation

3.6.1. Q and r Factor Measurements

Workbench measurements of the coil Q factor are performed by using the following:

$$Q = \frac{f_0}{B} \tag{14}$$

where f_0 represents the coil resonant frequency and B is the −3 dB coil bandwidth. The same equation can be used for both loaded and unloaded coil quality factor measurements and, successively, for r ratio estimation, according to Equation (6).

The quality factor measurements can be easily performed using a homemade dual-loop probe, consisting of a pair of pick-up loops and a network analyzer. The two circular loops of the probe are partially overlapped (distance between loop centers equal 0.75 times their diameter) to minimize the mutual coupling between the elements [33]; one loop is employed as a transmitter and the other one as a receiver. In this way, the TX loop is weakly coupled to the coil under test, which, in turn, is weakly coupled to the RX loop, with the result that the power transmitted to the RX loop is proportional to the amplitude of the oscillation in the coil under test, and therefore represents its frequency response [34].

3.6.2. Efficiency Measurement

Different magnetic field mapping methods, divided into electromagnetic bench tests and MRI techniques, can be used to estimate the coil efficiency at a fixed point, according to Equation (7). We tested the following four different methods: three methods for efficiency measurements using "probe techniques" (perturbing loop, perturbing sphere, and pick-up coil), and one NMR technique-based method.

3.6.3. Perturbing Loop Method

The perturbing loop method is based on adding a load consisting of an inductive loop of copper wire in series with a known resistance, R_L, placed inside the coil tuned at frequency, f (Figure 3a) [35].

The coil efficiency can be calculated as:

$$\eta = \sqrt{\frac{2R_L}{Q_{loop}/(Q_{load} - Q_{loop})}} \frac{1}{2\pi f S} \tag{15}$$

where Q_{load} and Q_{loop} are, respectively, the quality factor of the coil when loaded only with a sample and when loaded with both loads, and S is the loop area.

3.6.4. Perturbing Sphere Method

The perturbing sphere method involves inserting a metallic sphere inside the coil and successively measuring the frequency shift, f_1, caused by the sphere perturbation (Figure 3a) [36].

Then, the efficiency of the coil tuned at frequency f_0 can be estimated as:

$$\eta = \frac{1}{2}\sqrt{\left(\frac{\mu_0}{\pi^2 B_w r_s^3}\right)\left(\frac{f_1^2 - f_0^2}{f_0^2}\right)} \tag{16}$$

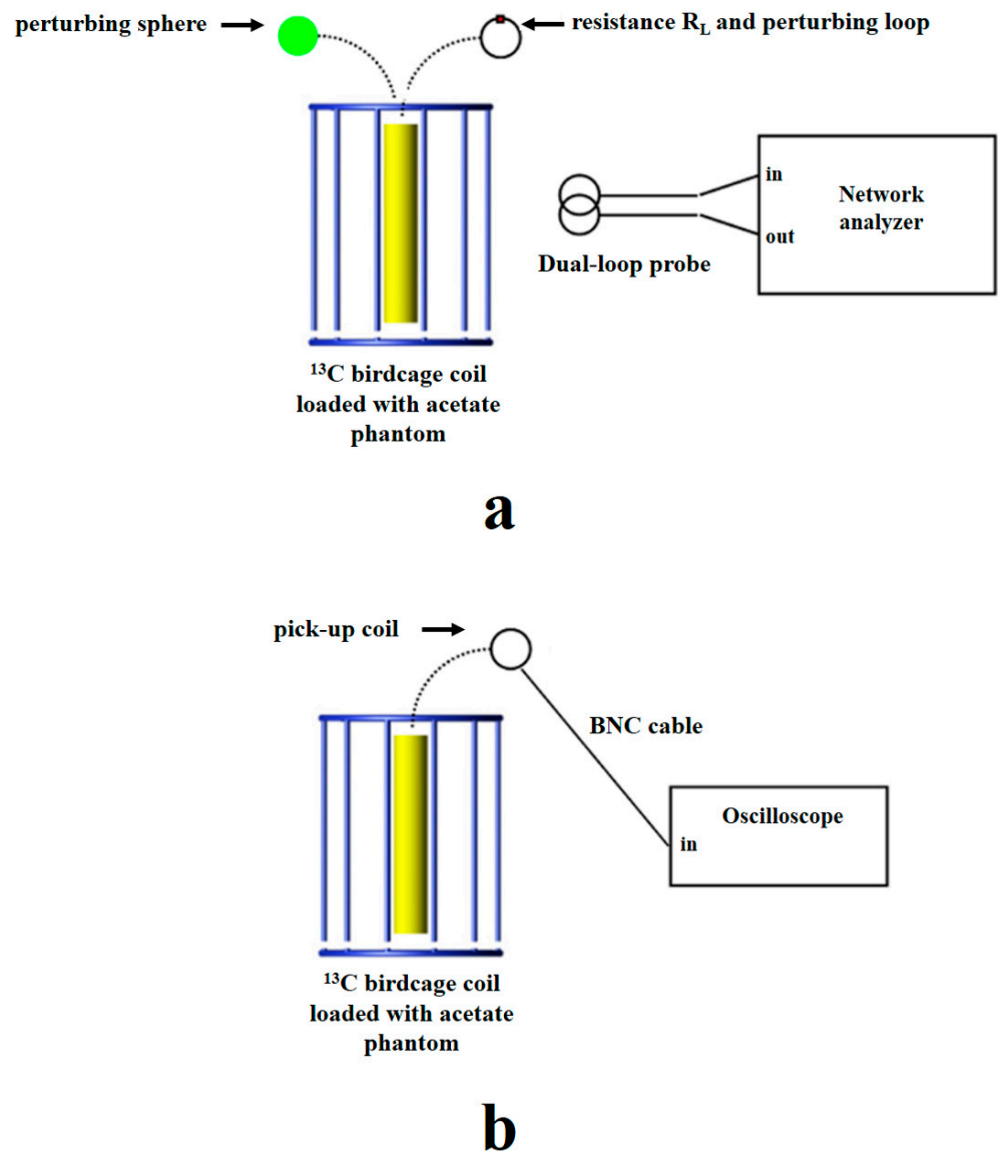where B_w is the −3 dB coil bandwidth and r_s is the sphere radius.

Figure 3. Experimental setups for workbench measurements. (**a**) Perturbing sphere and perturbing loop methods; (**b**) Pick-up coil method. Reprinted by permission from Giovannetti et al.,Measurement 2013 [37].

3.6.5. Pick-Up Coil Method

The pick-up coil method measures the magnetic field by detecting the current induced in a pick-up coil placed in an oscillating magnetic field of frequency, f (Figure 3b) [17]. If the pick-up loop of radius r is placed perpendicular to the direction of B_1 and V_{max} is the maximum voltage produced in the coil and measured with an oscilloscope, the following equation can be used to estimate the B_1 value as:

$$B_1 = \frac{V_{max}}{2\pi^2 r^2 f} \tag{17}$$

3.6.6. Nutation Experiment

The nutation method, which is the standard way of calibrating the B_1 field in MR experiments [38], consists of acquiring different spectrums with a linearly increasing pulse width.

The RF pulses change the magnetization orientation with respect to the static field direction, according to the rotational flip angle [39] as follows:

$$\theta = \gamma B_1 \tau \tag{18}$$

where γ is the gyromagnetic ratio (10.71 MHz/T for ^{13}C nucleus) and τ is the width in seconds of the RF hard pulse of amplitude B_1. By using Equation (17), the B_1 field of the coil can be estimated with the knowledge of the power that reaches the coil.

3.6.7. The Methods Tested on a 13C Coil

All described methods for coil efficiency estimation were verified with experimental measurements performed on a ^{13}C quadrature birdcage coil (4 cm radius, 12 cm length) tuned at 32.13 MHz and employed for ^{13}C metabolic studies on rats [40] and with a load consisting of a cylindrical phantom with dimensions 2.5 cm× 10 cm (diameter × length) containing 10 g [1-^{13}C]acetate, 58 mL H_2O, and 0.5 mmol Dotarem. Workbench tests were performed by using a homemade dual-loop probe and a network analyzer HP3577 (Hewlett Packard, Palo Alto, CA, USA).

For the perturbing loop method, five measurements were performed by using different RL resistance values (in the range of 39–470 Ω), for maximizing the measurement accuracy, and by using a 3 cm diameter loop placed in the coil volume. Measurements with the perturbing sphere method were performed by using a 6 mm radius lead sphere, and the efficiency value was calculated as the average of five measurements, while, for the pick-up coil method, the test was performed with a 2.5 cm radius pick-up loop connected to an oscilloscope (Tektronix THS720A, Tektronix, Beaverton, OR, USA).

Table 1 shows the coil efficiency values measured using the four methods, where the results obtained with workbench tests are reported as mean value ± standard deviation [37].

Table 1. Experimentally measured coil efficiency [37].

Coil	Perturbing Loop	Perturbing Sphere	Nutation	Pick-Up Loop
Coil efficiency in $\frac{\mu T}{\sqrt{W}}$	25.65 ± 1.76	26.40 ± 0.52	25.10	26.24

The differences between the measured values were below 5.2% as the maximum value, resulting in good agreement between the tested methods.

4. Software and Hardware for 13C Hyperpolarized Cardiovascular Magnetic Resonance (CMR) Experiments

Despite the increase in sensitivity, working with UHF scanners limits the clinical potential of hyperpolarized tracers; moreover, few groups have easy access to such facilities. Therefore, a convenient solution could be to enable the use of hyperpolarized tracers for clinical strength systems (1.5–3 T), with improved gradient performance and a powerful RF broadband amplifier. Therefore, acquisition protocols could be used that would be optimized for the clinic and dealing with tissue contrast and relaxation times typical of human studies, thus, fostering translation of the results.

Over the last years, several chemical shift imaging (CSI) and MRS strategies have been developed and optimized to perform acquisition of the hyperpolarized spectroscopic

signal with high temporal and spatial resolution, also taking into account that RF pulses contribute to depleting the hyperpolarization [8,9].

Single or multi-slice free induction decay (FID)-CSI with low flip-angle excitation is among the first acquisition protocols proposed for in vivo experiments. It is a robust and easy way to implement the method for the acquisition of broad spectral bandwidth; however, it provides an inefficient encoding scheme [41,42]. Variable flip-angle schemes can be used to further improve the SNR and metabolite signal detection [43]. FID-CSI approaches are suitable for tracking the real-time metabolic conversion of the injected hyperpolarized substrate, from which semi-quantitative kinetic parameters (e.g., kinetic constants of metabolic conversion) can be extracted [44,45]. Mapping the in vivo distribution of the hyperpolarized species is usually performed using single-shot acquisitions that improve temporal and spatial resolution while preserving the hyperpolarization. Spiral trajectories [46], often associated with multi-echo chemical shift species separation methods, such as in IDEAL spiral CSI [47], or spectral-spatial excitation [48], provide efficient k-space coverage for rapid detection of the hyperpolarized spectroscopic signal over the anatomic volume of interest [49]. Acceleration protocols, such as Echo-Planar Spectroscopic Imaging (EPSI) [50,51], compressed sensing [52,53] or parallel imaging [54,55], have been proposed to fasten the detection of the hyperpolarized signal.

As an alternative, methods based on the achievement of a pseudo steady-state magnetization, such as in balanced steady-state free precession (bSSFP) [56,57], have also been implemented, providing good spectral selectivity and reduced scan time.

A comprehensive overview of acquisition sequences is beyond the scope of this paper, while a more detailed analysis can be found, for instance, in the recent paper by Topping et al. [58].

4.1. Dedicated Coil Development for Clinical Scanners

In general, safety and compatibility criteria must be satisfied in the design of all new devices used inside an MR scanner.

The dedicated RF coils have to be designed to be compatible with commercial scanners because they have to be connected to the scanner, and generally, the interconnection is achieved via 50 Ω coaxial cables, whose shield design and dielectric material quality permit the transport of the RF energy as low-loss lines.

Cables that are not well terminated in their characteristic impedance may be subjected to common mode currents and standing waves, which could create heating to the patient/sample and irradiated energy in the surroundings. Moreover, different MR scanners could use various and proprietary connectors, so that a strong collaboration between researchers and scanner manufacturers is always required.

Coils have to be matched to 50 Ω for optimizing the energy transfer through all parts of the spectrometer, since the system impedance is a pure 50 Ω resistance, and different impedance matching circuits can be specifically designed for MR applications, generally consisting of inductors and/or capacitors [59].

Generally, coil prototypes designed to be used in transmit/receive mode with clinical scanners employ a T/R switch inserted between the coil and the scanner, normally provided by a scanner manufacturer, which monitors the specific absorption rate (SAR) to avoid harming the sample.

Finally, capacitors and diodes, usually employed as switching devices included in the coil design, are obtained commercially, and many manufacturers provide them in a nonmagnetic version, specially designed for MR applications. Although, in some cases, the inductors can be home built, very small dimension nonmagnetic inductors are commercially available.

4.2. ^{13}C Coils in Our Lab: Design, Simulation, and Test

4.2.1. TX/RX Surface Circular Coil

A 25 cm diameter circular coil, built using a 1 cm width strip copper conductor, was designed for investigating the pig heart [60], which extends from 2 to 12 cm in depth with respect to the coil plane, according to the theory which suggests matching the coil radius with the desired imaging depth [6]. The Biot–Savart equation, Equation (9), was employed for the three-dimensional B_1 field distribution evaluation, while coil inductance ($L = 0.673$ µH) was calculated by adapting Equation (3) to the coil geometry.

Coil losses ($R_{coil} = 57$ mΩ) and sample-induced resistance ($R_{sample} = 1.58$ Ω) were calculated by using Equations (10) and (13), respectively, and by using a load consisting of a pair of cubic samples with dielectric properties defined following the American Society for Testing and Material criteria for MR phantom development ($\varepsilon_r = 78$, $\sigma = 0.39$ S/m) [61], which was employed for all the simulations described in this paper. After the simulation, a prototype of the circular coil was designed and built, according to the scheme of Figure 4a.
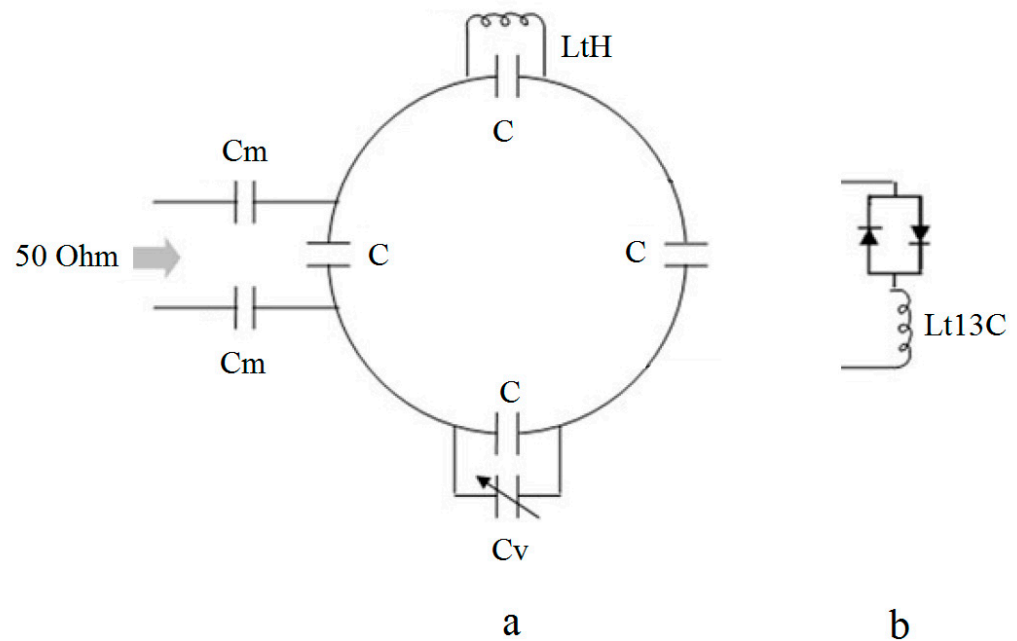

Figure 4. (**a**) TX/RX circular coil; (**b**) Decoupling circuit for the RX-only circular coil.

C represents the high-quality capacitors (ATC 100C—American Technical Ceramics, Huntington Station, NY, USA) employed for the coil tuning at $f_0 = 32.13$ MHz, while C_v is a variable capacitor (AP40HV Voltronics, Voltronics, Salisbury, MD, USA) useful for the coil fine-tuning within the MR system.

C_m represents a capacitive circuit for matching the coil impedance to 50 Ω resistance in order to employ coaxial cable optimally without added losses, which can be calculated as [27]:

$$\frac{1}{2}C_m = \sqrt{\frac{C}{2\pi f_0 Q 50}} \tag{19}$$

where Q is the coil quality factor. In particular, C_m are the matching capacitors whose negative reactance cancels the positive reactance of the coil inductance and with the C tuning capacitor transform the coil resistance to a pure 50 Ω at the Larmor frequency of 32.13 MHz.

Since the circular coil was designed as TX/RX coil at ¹³C frequency and the whole-body coil was employed for 1H imaging (anatomical localization), a decoupling circuit was added to the circuit coil to eliminate the interactions between the ¹³C and the 1H coil. This resonant blocking circuit L_{tH}-C is tuned at 1H frequency (128 MHz): any voltage induced by the 1H coil in the ¹³C coil is blocked by the resonant circuit L_{tH}-C, while when the 1H coil is switched off, the ¹³C coil is tuned correctly.

For coil testing to evaluate the SNR for hyperpolarized substances, we acquired a chemical shift imaging (CSI) of a hyperpolarized [1-¹³C]pyruvate phantom with a 3T GE Excite HDx (GE Healthcare, Waukesha, WI) scanner, which was employed in all the experiments described in this paper, and using an elliptic FIDCSI sequence with the following parameters: FOV 120 mm, 16 × 16 matrix with reduced k-space sampling (208 phase encoding steps), 256 points, slice thickness 2 cm, FA 30°, TR 80 ms, and bandwidth 5000 Hz.

Figure 5b shows the comparison between the theoretical SNR profile, calculated with Equation (8), and the experimental SNR profile extracted from the map acquired with CSI of a hyperpolarized [1-¹³C]pyruvate phantom (Figure 5a), underlying the good agreement between theoretical and measured SNR provided by the coil.

The SNR on CSI data, for developing the profile shown in Figure 5b, was evaluated as SNR = Sp/σn, where Sp is the real part of the spectrum maximum peak and σn is the standard deviation of the last points of the spectrum where only noise is present.

The SNR profile in Figure 5b is obtained from the CSI voxels outlined with a dotted line in Figure 5a; the maximum value of SNR is obtained at 2 cm in depth from the coil, according to the coil design.
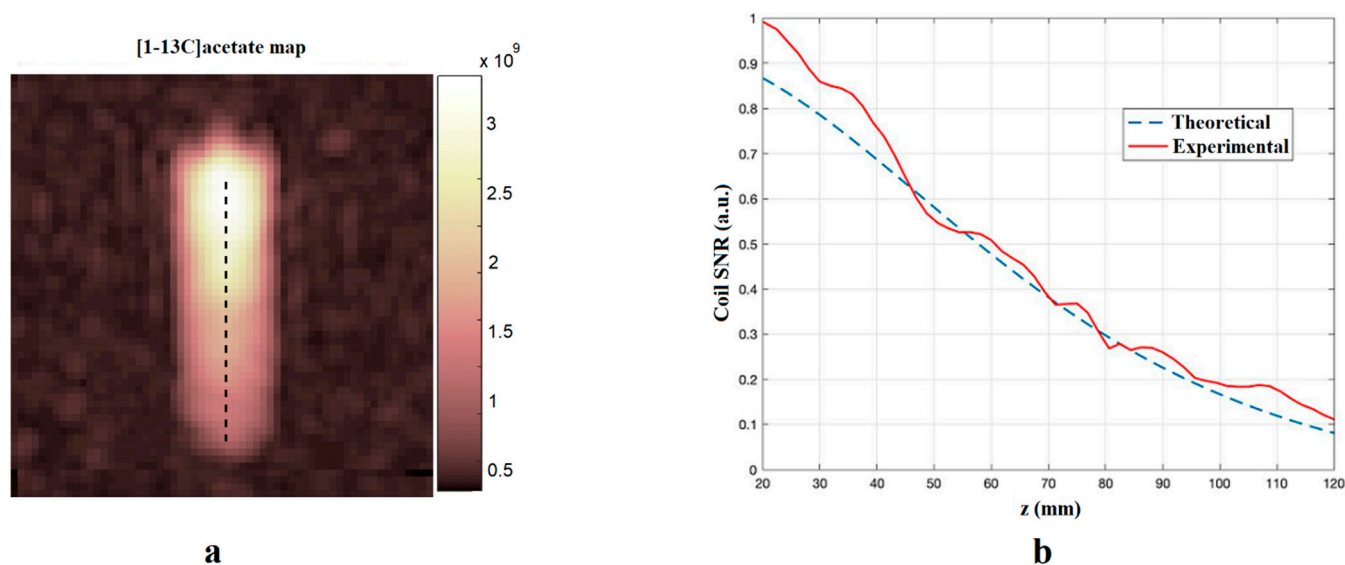

Figure 5. (**a**) [1-¹³C]acetate map, the dotted line shows which voxels are used to define the experimental SNR profile of Figure 4b; (**b**) Theoretical and experimental (along the line indicated in the phantom) SNR profiles [60].

4.2.2. TX/RX Volume Birdcage Coil

The circular surface coil, described in the previous paragraph, was compared with a volume coil constituted by a ¹³C birdcage coil (Rapid Biomedical, Wurzburg, Germany) in low-pass version (radius of 18.2 cm, length of 36 cm, n = 12 legs) used for pig experiments [18].

The birdcage losses, consisting of 1 cm width strip conductors for the end-ring conductors and 0.5 cm radius wire for the leg conductors, were calculated with Equation (10), giving a value of 0.36 Ω. In parallel, the sample-induced resistance for the coil loaded with the same phantom, described in Section 4.2.1, can be calculated using Equation (13), re-

sulting in a value of 1.05 Ω. The birdcage inductance (0.423 µH) was estimated by considering the ''global'' inductance of the coil [62] by schematizing the conductors with a transmission line [63]. The magnetic field distribution was computed with the FDTD method, which permitted numerical evaluation of the B_1 value for each point inside the sample.

Figure 6 depicts the profile plot of the magnetic field pattern dependence on the depth profile for the circular and birdcage coil. The high magnetic field homogeneity of the birdcage coil is evident from Figure 6, while the circular coil B_1 field falls off rapidly.
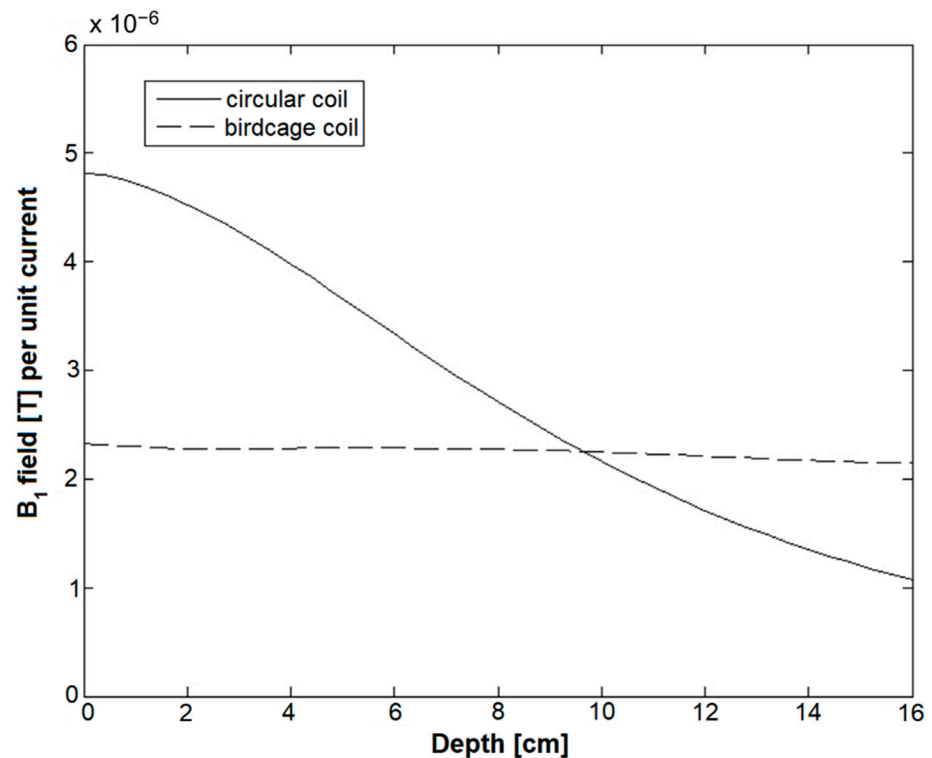

Figure 6. Comparison of the magnetic field patterns for the circular and the birdcage 13C coils. Adapted by permission from Giovannetti et al., App Magn Reson 2012 [18].

The two coils were successively compared with an in vivo experiment on a pig model, by using the previously described sequence parameters but with TR = 3 s. Two administrations of hyperpolarized [1-^{13}C]pyruvate were made on the pig: one to acquire data with the circular coil and the other to acquire data with the birdcage coil; about an hour had passed between the two administrations. The single spectrum acquired with circular (Figure 7a) and birdcage (Figure 7b) coils on the pig heart revealed a significant increase in the signals obtained using the circular coil because the selected region is close to the coil plane.
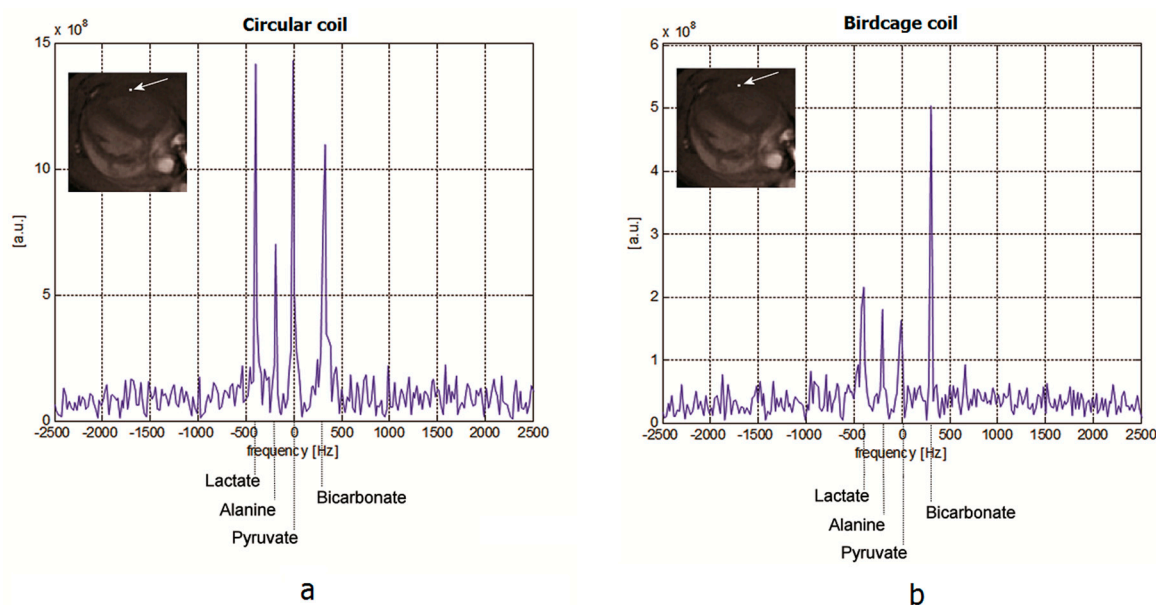
Figure 7. Hyperpolarized ^{13}C spectra acquired with the circular coil (**a**) and the birdcage coil (**b**). Adapted by permission from: Giovannetti et al., App Magn Reson 2012 [18].

4.2.3. TX Volume Birdcage Coil/RX Surface Circular Coil

After the design and test of the circular and birdcage coils, both employed as TX/RX coils, we studied a "hybrid" configuration for exploiting the advantages of each coil design. This setup comprised, therefore, the use of two different coils: a transmit coil, constituted by a homogeneous volume resonator for achieving an efficient excitation in a large volume, and a receive coil, characterized by a high local sensitivity [64].

Since this novel surface coil had to be employed as RX-only coil, we added a passive decoupling circuit to the loop as depicted in Figure 4b, constituted by the series of L_{t13C} inductance and back-to-back diodes which were fixed in parallel to C capacitance: during the TX phase, a current in the diodes is induced by the voltage across the circuit, and the parallel resonant circuit acts as a high impedance, while the surface coil is tuned correctly when the TX coil is switched off. The volume birdcage coil was also modified for being used as a TX-only coil, by adding an active decoupling circuit using PIN diodes biased by an external circuit synchronized with the pulse sequence.

The hybrid coil was tested in vivo to obtain metabolic information on a pig heart by using an IDEAL spiral CSI (axial plane, FOV = 30 cm, slab thickness = 10 cm, 11 constant echo time shift of TE = 0.9 ms, FA = 7°, 14 phase encoding steps along the z-direction), based on single-shot spiral image encoding and echo time.

The hybrid coil resulted in a good representation of the pyruvate signal in both ventricular cavities (Figure 8), although a slight signal increase was visible in the left ventricle cavity and in the superior part of the right ventricle, close to the circular coil, placed in the superior part of the pig. The bicarbonate map was also clearly visible in the whole left ventricle (LV) wall closest to the circular coil.
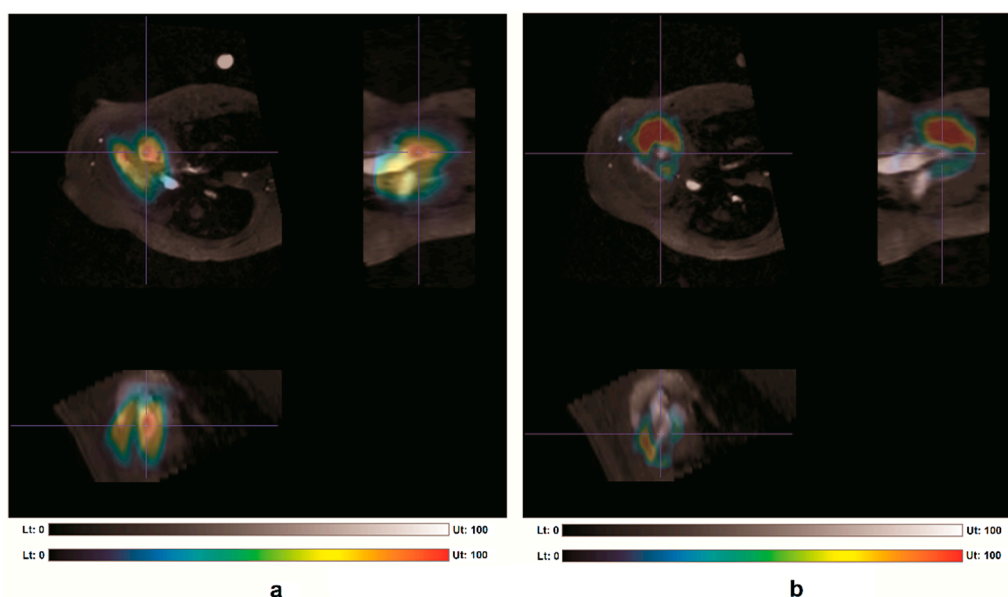
Figure 8. Hyperpolarized [1-^{13}C]pyruvate and [1-^{13}C]bicarbonate maps evaluated from chemical shift imaging (CSI) with the hybrid coil. (**a**) Pyruvate signal; (**b**) Bicarbonate signal. Reprinted by permission from Giovannetti et al., *App Magn Reson* 2013 [64].

4.2.4. Quadrature Surface Coil in TX/RX and RX Only

The design of a novel surface coil configuration arose from the necessity to improve the SNR provided by the circular coil. We combined two coils into a quadrature surface coil, which was able to produce orthogonal B_1 fields in a restricted region and to provide an SNR improvement by a factor of up to $\sqrt{2}$. The first coil was the same circular coil previously described, while the second was an anti-symmetric two-loop coil (butterfly), in which the currents flowing in its conductors generate a B_1 field that, in the central region of the coil, is a transverse RF field [65].

The butterfly coil sizes were selected to provide overlapping with the circular coil and to guarantee good symmetry between the two coils (see Figure 9a, where A = 11.5 cm, B = 2 cm, and H = 25 cm). Successively, the mutual coupling between the butterfly and the circular coil was minimized by adjusting the overlapping region of the two coils.
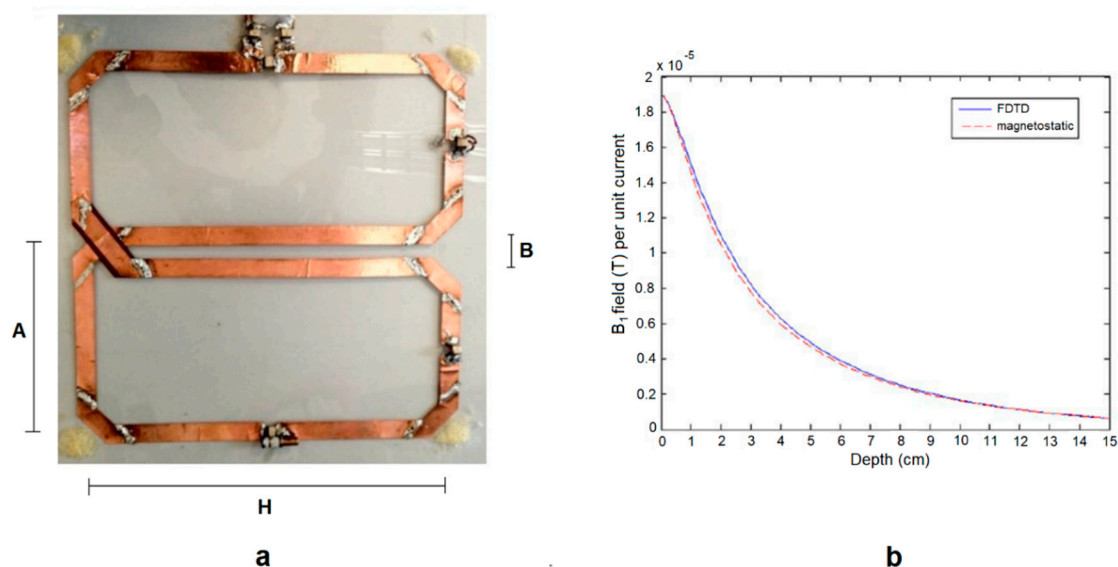

Figure 9. A butterfly coil. (**a**) Prototype picture; (**b**) Magnetic field pattern calculated with the finite-difference time-domain (FDTD) and magnetostatic methods. Adapted by permission from Giovannetti et al., Measurement 2013 [66].

The FDTD method was used for evaluating the B_1 value of each point inside the sample and for calculating sample-induced resistances according to the algorithm described in Section 3.4.4.

The xFDTD (Remcom, State College, PA, USA) software was used to perform the numerical simulations. A 1 V amplitude Gaussian pulse with a suitable frequency spectrum around the coil resonant frequency was used to excite the coils and the PEC type was assigned as coil material. For truncating outward waves and simulating computational domain infinite radiation boundary conditions, a perfect matched layer (PML) was used. Moreover, the simulations were performed with the coils loaded with the previously described phantom (Section 4.2.1) and by using a nonuniform mesh, with the mesh distribution design on a region-by-region basis.

The butterfly coil inductance was calculated using Equation (3) and was 1.059 µH, while the coil resistance and the sample-induced resistance, respectively, were calculated using Equations (10) and (13), and provided values of 0.25 Ω and 1.77 Ω.

For comparison purpose, the magnetic field patterns along with the depth profile for the butterfly coil was estimated by magnetostatic analysis and the FDTD tool, and the simulations provided very similar values (Figure 9b), demonstrating that the magnetostatic assumption is valid at the 13C frequency, since the radiation wavelength is 9.4 m at 32.13 MHz in free space, which is much greater than the coil dimensions.

The quadrature surface coil, consisting of a combination of the butterfly and the circular coil, was previously designed and tested as TX/RX configuration. The obtained SNR was higher as compared with the SNRs provided by the single coils in a wide range of the penetration depth into the phantom (Figure 10), while the MR acquisition of metabolic maps with hyperpolarized [1–13C]pyruvate injected in a pig showed that the configuration was able to effectively image the hyperpolarized [1–13C]pyruvate distribution, Successively, the same quadrature surface coil was used in RX mode in combination with a birdcage coil as a transmitter [66]. For this purpose, a passive decoupling circuit was added to both surface coils, as described in a previous paragraph. The SNR profile of this TX birdcage/RX quadrature coil configuration underlined its advantage in a wide range of coil-to-voxel distances (Figure 10).
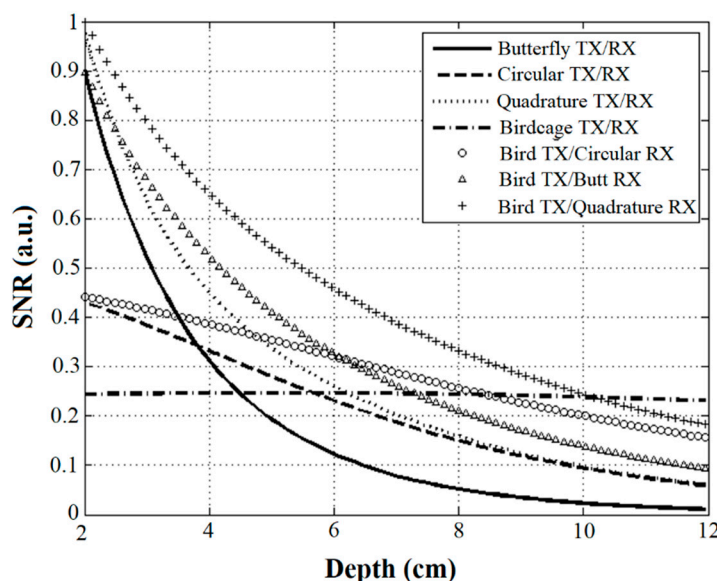

Figure 10. Theoretical SNR profiles obtained for ^{13}C coils with different geometries and in different configurations. Reprinted by permission from Giovannetti et al., Measurement 2015 [67].

4.2.5. Theoretical Comparison between 13C Coil SNR Plots

A successive work [67], comparing 13C coils with different geometries (circular, butterfly, birdcage, and quadrature surface coils) employed in single element TX/RX mode and in combination with different setups (transmit-only birdcage coil and receive-only surface coil, again called "hybrid" configurations), was performed with the SNR model previously described.

The theoretical SNR trends of dependence on the depth profile along the sample region (from 2 to 12 cm) are shown in Figure 10 for all coil configurations.

The TX/RX circular coil is characterized by its inhomogeneous B_1 field distribution, which decreases strongly with the distance from the coil plane, while the TX/RX butterfly coil shows a more rapid decay as the observation point moves away from the coil plane, although the SNR values in the first 2 cm of the phantom extension are higher than the circular coil ones.

It is well known that the birdcage produces a highly uniform magnetic field, and the SNR trend of the TX/RX birdcage coil is almost constant with respect to the depth profile.

The TX/RX quadrature configuration provides higher SNR with respect to the single TX/RX circular and TX/RX butterfly coil configurations in a wide range of penetration depths of the phantom length. Regarding the hybrid configurations, their theoretical SNR profiles underlined their advantage over the TX/RX single coils in the entire penetration depth of the phantom. Finally, the TX birdcage/RX quadrature coil configuration outperforms the TX/RX birdcage in a wide range of coil-to-voxel distances (80% of the phantom extension).

4.2.6. 16-Channel Array Coil

A 16-channel receive surface array coil was designed for 13C hyperpolarized studies of the pig heart with the same clinical scanner [68]. Each elliptic element in the coil was 5 × 8 cm^2 with a conductor width of 2 mm (Figure 11).
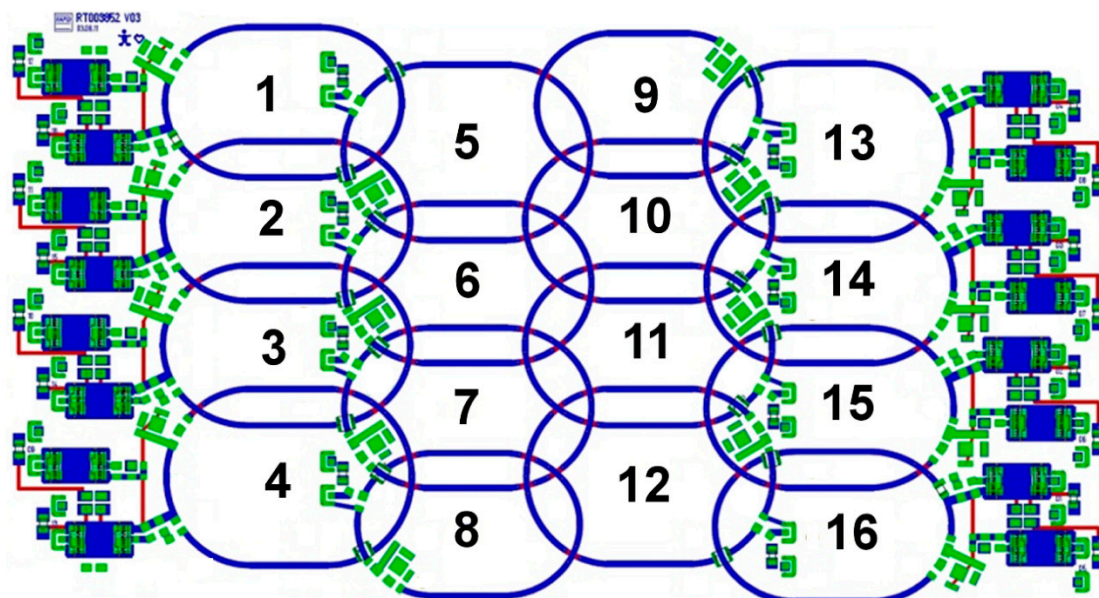

Figure 11. Phased-array coil structure. Reprinted by permission from Frijia et al., *Journal of Medical and Biological Engineering* 2016 [68].

Symmetric coupling schemes, including cable traps were used to fix tuning and matching, while active decoupling was performed by PIN diodes within 13C traps and passive 1H traps were used for decoupling the resonator and wiring from the 1H body

coil. Preamplifier decoupling was achieved by transforming the high S11 of the preamplifier input to a high impedance in the coil circuit by phase shifters. Animal studies on six healthy male mini pigs were performed to test the coil. The metabolic maps of pyruvate, lactate, and bicarbonate (Figure 12) were obtained with three-dimensional (3D) imaging sequence on the heart, performed with a stack of axial plane single-shot spiral trajectories, FOV = 30 cm, a nominal resolution of 8 mm, and a duration of 42 ms using the maximal gradient strength of 40 mT/m and maximal slew rate of 150 T/m of the system.
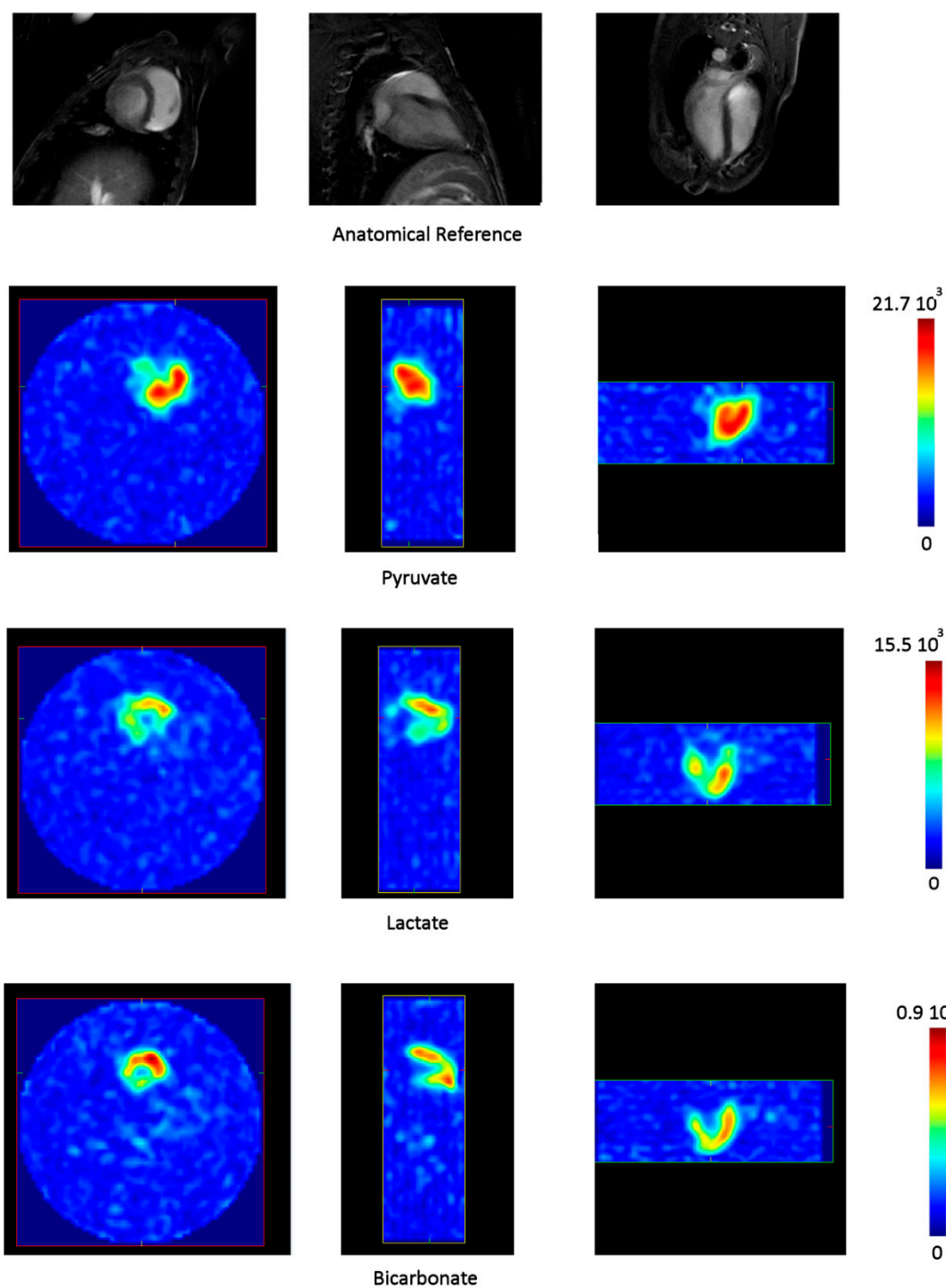

Figure 12. Triplanar views of pyruvate, lactate, and bicarbonate on three main heart axes. Reprinted by permission from: Frijia et al., *Journal of Medical and Biological Engineering* 2016 [68].

With respect to the previously described coil configurations, a significant improvement of SNR in the heart wall near the coil surface was obtained using the 16-channel coil. The SNR was also acceptable in the remote heart wall, allowing assessment of cardiac metabolism in the whole heart.

4.2.7. 1H solenoid/13C Circular Coil for Small Animal Studies

Acquisition in a mouse model was performed after the design and simulation of a dual-tuned RF coil configuration operating at two frequencies of interest (1H of 127.75 MHz and 13C of 32.13 MHz), constituted by a 1H whole body solenoid coil for imaging and a 13C circular loop surface coil for performing 13C acquisitions, with both coils employed in TX/RX with a 3T scanner [69].

The 1H volume coil (Figure 13a) is a solenoid (12 cm length, 4.4 cm diameter, 20 turns), characterized by the possibility of achieving high magnetic field homogeneity in both transversal and longitudinal sections.
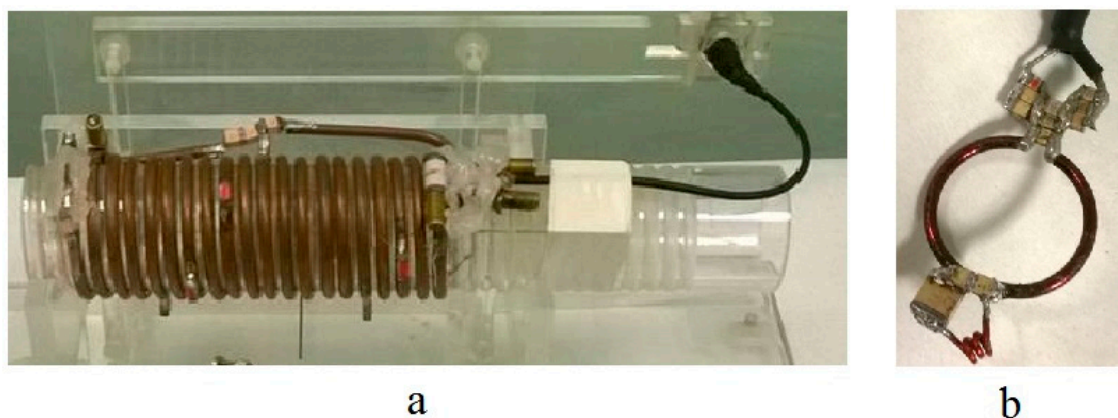

Figure 13. RF coils for hyperpolarized 13C studies in small animal models, to be integrated with the clinical scanner. (**a**) 1H solenoid; (**b**) 13C circular coil.

The spacing between turns was chosen to achieve the best compromise between magnetic field homogeneity and minimization of losses due to proximity effect [70], resulting in an optimum spacing of sp = 3 a [71], where a is the wire radius = 2 mm.

The 13C surface coil (Figure 13b) is a 2.5 cm diameter circular loop built with a 2 mm diameter wire conductor and decoupled by the 1H solenoid using a resonant blocking circuit tuned at proton frequency and consisting of an LCC trap [72].

For both coils, the magnetic field distribution was calculated with the Biot–Savart equation and inductance by adapting Equation (3) to the coil geometries, resulting in values of 5.256 μH for the solenoid and 40.97 nH for the circular coil.

Coil workbench tests consisted of Q and r measurements, according to Equations (14) and (6), respectively, and the results are shown in Table 2. The r values underlined that for the solenoid, the losses are mainly caused by the sample load. In contrast, as expected for surface coils, the circular coil contribution to the signal loss is determinant.

Table 2. The workbench results obtained for the two coils [69].

Coil	$Q_{unloaded}$	Q_{loaded}	r
1H solenoid	259	47	5.51
13C circular	168	114	1.47

With this coil configuration it was possible to obtain both anatomical and metabolic information within the same study session. For the in vivo experiment, a healthy mouse

was placed at the center of the 1H solenoid, and the 13C circular coil was positioned adjacent to the back of the mouse, in relation to the heart. Anatomical proton images were acquired with a fast spin-echo (FSE) sequence (FOV = 8 × 8 cm^2, 512 × 512 matrix, FA = 90°, TE/TR = 2800/67.488 ms).

The ^{13}C spectroscopic signal was detected by using IDEAL spiral CSI (FOV = 8 × 8 cm^2, TR = 1000 ms, echo times = 7, echo spacing = 1.12 ms, scans = 32, and flip-angle = 10°), from a 10 mm axial slice selected to include the heart, liver, and kidney in the field of view.

The metabolic maps of the spatial distribution of hyperpolarized [1-^{13}C]pyruvate obtained in vivo and overlapped on reference anatomical images are shown in Figure 14.

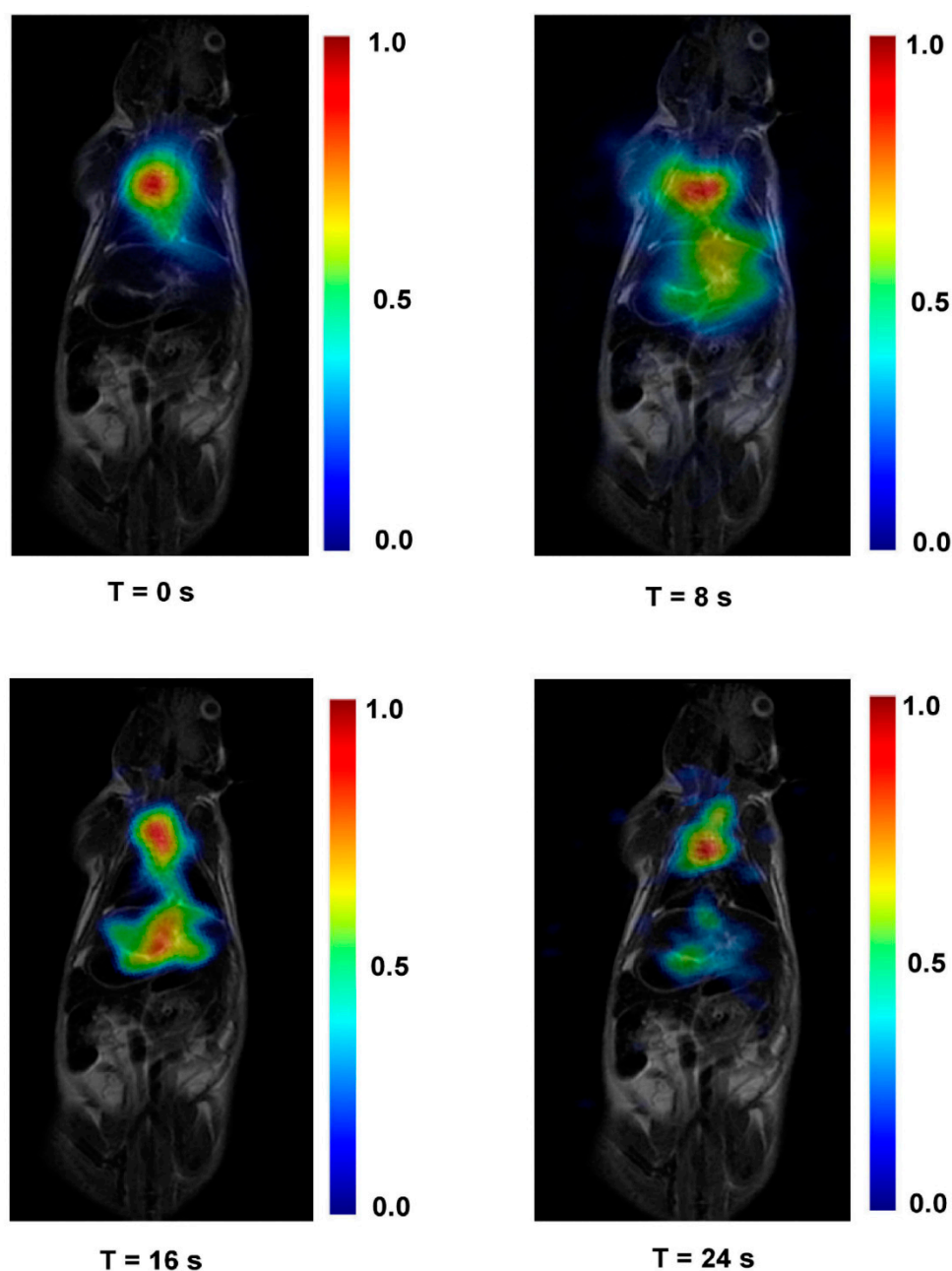**Figure 14.** Metabolic maps of spatial distribution of hyperpolarized [1-^{13}C]pyruvate obtained in vivo and in real time with a time step of 8 s, overlapped on reference anatomical images. Reprinted from *Scanning* 2016 [69].

5. Discussion

In recent years, a new methodology based on MRS using hyperpolarized ¹³C has been demonstrated to be useful for studying cardiac metabolism in animal models. Although small animal models, for example, rodents, could help to understand human cardiac pathophysiology, rodent and human hearts differ in many important aspects, such as anatomy, heart rate, oxygen consumption, and contractility. Hence, the use of large animal models, such as the pig, could be preferable as pigs and humans have similar cardiac size, physiology, and coronary anatomy. Large animal models could be imaged on UHF MR scanners, with an expected increase in the SNR. Unfortunately, the use of UHF scanners requires several problems to be addressed, such as magnetic field inhomogeneity, off-resonance artifacts, dielectric effects, RF nonuniformities, and synchronization of data acquisition with the cardiac cycle using a conventional ECG [73]. Moreover, the use of large-bore UHF scanners is limited to a few centers due to high installation and maintenance costs. Hence, experiments on large animal models are usually performed on high field MR clinical systems (1.5–3.0 Tesla). The development of dedicated RF coils represents a key issue for a successful experimental setting in MR clinical systems. In fact, the development of ¹³C-specific RF coils is challenging due to the lower resonance frequency of the ¹³C nuclei and the integration with existing 1H coils. Small differences in coil losses could even have an impact on SNR, as the coil operates at a frequency where electronic noise cannot be neglected. The tradeoff between achieved SNR and signal homogeneity is the key issue in RF coil design. In most hyperpolarized ¹³C heart studies, the anatomical region of interest corresponds to the left ventricle wall, as most of the heart pathologies are related to regional dysfunctions of the LV myocardium. For instance, coronary stenosis or occlusion leads to a perfusion defect in some LV wall segments, depending on the affected coronary vessel [74].

Hence, cardiac imaging techniques should provide a uniform sensitivity in the whole LV wall. In addition, the sensitivity of ¹³C imaging should be high enough to detect the signal related to derivate metabolites, which in certain cases could be low due to the reduced flux of conversion [75]. The design of the RF coil configuration to be used in cardiac ¹³C experiments should take into account both of these aspects.

As shown in Figure 6, birdcage coils assure a uniform SNR value among the FOV, while surface coils provide a higher SNR value near the coil with a rapid decrease in the distance. MRS experiments on pig heart confirmed the signal gain obtained by surface coils (Figure 7). Hybrid coils, composed of a birdcage transmit coil, are able to achieve an efficient excitation in a large volume, and a planar receive coil, characterized by high local sensitivity, could represent an effective compromise between signal homogeneity and high SNR (Figure 8). The SNR value could be further enhanced by appropriate surface coil design (Figure 10). The use of phased array coils (Figure 11) built by combining several elements further increases the SNR value attempting to preserve signal homogeneity (Figure 12). The flexible design of the coil allowed detection of the signal in the whole myocardium. However, the signal intensity was significantly different among LV segments, and therefore measuring segmental signal variations could be challenging as variations induced by coil geometry may mask "true" variations induced by physiological changes.

Finally, an appropriate coil design (Figure 13) could enable performing experiments on small animals on high field MR clinical scanner (Figure 14). Although a clinical scanner cannot match the performance of a small animal MRI scanner, small animal imaging could be useful during the setup of the experimental protocols limiting the use of large animal models.

6. Conclusions

Cardiac function noninvasive assessments can be achieved by tissue metabolic state studies with MRS. In particular, hyperpolarized ¹³C-labeled pyruvate has been utilized to

monitor the metabolism of biomolecules for normal and dysfunctional myocardium. However, the weak nuclear polarization and the low natural abundance can reduce the MR experiment sensitivity, producing low signal in MRS, and although hyperpolarization methods have been proposed for enhancing the polarization of nuclear spins such as ^{13}C, the design and development of dedicated RF coils is a fundamental task. Such transmit and receive coils, operating at the ^{13}C frequency (32.13 MHz at 3T), have to provide the desired FOV and an optimal SNR.

The correct design and realization of RF coils represent a key issue in the effective setting of ^{13}C experiments on a high-field clinical scanner. Depending on the physiological question to be answered, the coil used should implement the correct tradeoff between SNR gain and signal uniformity over the area of interest.

Starting from the RF coil theoretical principles, in this paper, we described coil performance parameters and their estimation methods in the coil development for various phases (simulations, workbench tests, and MR experiments).

Thereafter, we summarized the experience of our cardiovascular laboratory in the simulation, design, and testing of different coil arrangements (circular, butterfly, birdcage, and receive arrays) for hyperpolarized ^{13}C studies of pig and mouse heart with a clinical 3T scanner.

In particular, such different ^{13}C coil configurations were initially simulated for developing an SNR model geometrical distribution by computing the coil resistance, the sample-induced resistance, and the magnetic field pattern for each coil. While coil resistance was calculated from Ohm's law, sample induced resistances were estimated using a FDTD algorithm and magnetic field with magnetostatic theory and FDTD.

The main objective of the paper was to present a significant example of the work carried out at an electromagnetic laboratory in the field of RF coil design, building, and testing. Table 3 reports the technical details of materials, equipment, and tools employed in our laboratory focused on cardiovascular research. This aspect may represent a limitation, as a single MR 3T scanner was used and other anatomical districts were not investigated. However, the RF coils, presented in this paper, effectively cover the range of the main coil types employed in the cardiac ^{13}C research field.

Table 3. List of equipment and methods employed for the simulation and test of the different homemade coils. The inductors of the decoupling traps were handmade by using copper wire. RG-58 coaxial cables were employed for coils connection. Workbench tests were performed by using a homemade dual-loop probe and a network analyzer HP3577 (Hewlett Packard), while MR tests were performed with a 3T GE Excite HDx (GE Healthcare, Waukesha, WI, USA) scanner.

Coil	Conductor	Capacitor	Simulation Software
[13]C TX/RX surface circular coil for pig experiments [60]	1 cm width and 70 μm thickness strip	-ATC 100C (American Technical Ceramics, USA) for fixed capacitors -AP40HV (Voltronics, USA) for variable capacitor	-Homemade program based on IDL 6.0 (Interactive Data Language, Visual Information Solutions, Boulder, CO, USA) for inductance and magnetic field calculation -GEMS simulator (EMC Lab, Pennsylvania State University, PA, USA) for sample-induced resistance calculation
[13]C RX surface circular coil for pig experiments [64]	1 cm width and 70 μm thickness strip	-ATC 100C (American Technical Ceramics, USA) for fixed capacitors -AP40HV (Voltronics, USA) for variable capacitor	-Homemade program based on IDL 6.0 (Interactive Data Language, Visual Information Solutions, Boulder, CO, USA) for inductance calculation -xFDTD tool (Remcom, PA, USA) for magnetic field and sample-induced resistance calculation
[13]C TX/RX and RX only butterfly coil for pig experiments [65,66]	1.2 cm width and 70 μm thickness strip	-ATC 100C (American Technical Ceramics, USA) for fixed capacitors -AP40HV (Voltronics, USA) for variable capacitor	-Homemade program based on IDL 6.0 (Interactive Data Language, Visual Information Solutions, Boulder, CO, USA) for inductance and magnetic field calculation -xFDTD tool (Remcom, PA, USA) for magnetic field and sample-induced resistance calculation
1H TX/RX solenoid for mouse experiments [69]	2 mm radius wire	-ATC 100C (American Technical Ceramics, USA) for fixed capacitors -AP40HV (Voltronics, USA) for variable capacitor	-Homemade program based on MATLAB (The Mathworks, Natick, MA, USA) for inductance and magnetic field calculation
[13]C TX/RX surface circular coil for mouse experiments [69]	1 mm radius wire	-ATC 100B (American Technical Ceramics, USA)	-Homemade program based on MATLAB (The Mathworks, Natick, MA, USA) for inductance and magnetic field calculation

References

1. Santarelli, M.F.; Positano, V.; Martini, N.; Valvano, G.; Landini, L. Technological Innovations in Magnetic Resonance for Early Detection of Cardiovascular Diseases. *Curr. Pharm. Des.* **2016**, *22*, 77–89, doi:10.2174/1381612822666151109112240.
2. Santarelli, M.F.; Martini, N.; Positano, P.; Landini, L. Models and Methods in Cardiac Imaging for Metabolism Studie. *Curr. Pharm. Des.* **2014**, *20*, 6171–6181, doi:10.2174/1381612820666140417114122.
3. Van Ewijk, P.A.; Schrauwen-Hinderling, V.B.; Bekkers, S.C.A.M.; Glatz, J.F.C.; Wildberger, J.E.; Kooi, M.E. MRS: A noninvasive window into cardiac metabolism. *NMR Biomed.* **2015**, *28*, 747–766, doi:10.1002/nbm.3320.
4. Shulman, R.G.; Rothman, D.L. 13C NMR of intermediary metabolism: Implications for systemic physiology. *Annu. Rev. Physiol.* **2001**, *63*, 15–48, doi:10.1146/annurev.physiol.63.1.15.
5. Ardenkjaer-Larsen, J.H.; Fridlund, B.; Gram, A.; Hansson, G.; Hansson, L.; Lerche, M.H.; Servin, R.; Thaning, M.; Golman, K. Increase in signal-to-noise ratio of >10,000 times in liquid-state NMR. *Proc. Natl. Acad. Sci. USA* **2003**, *100*, 10158–10163, doi:10.1073/pnas.1733835100.
6. Haase, A.; Odoj, F.; Von Kienlin, M.; Warnking, J.; Fidler, F.; Weisser, A.; Nittka, M.; Rommel, E.; Lanz, T.; Kalusche, B.; et al. NMR probeheads for in vivo applications. *Concepts Magne. Reson.* **2000**, *12*, 361–388, doi:10.1002/1099-0534(2000)12:6.
7. Sánchez-Heredia, J.D.; Olin, R.B.; McLean, M.A.; Laustsen, C.; Hansen, A.E.; Hanson, L.G.; Ardenkjær-Larsen, J.E. Multi-site benchmarking of clinical 13C RF coils at 3T. *J. Magn. Reson.* **2020**, *318*, 106798, doi:10.1016/j.jmr.2020.106798.
8. Skinner, J.G.; Menichetti, L.; Flori, A.; Dost, A.; Schmidt, A.B.; Plaumann, M.; Gallagher, F.A.; Hövener, J.-B. Metabolic and Molecular Imaging with Hyperpolarised Tracers. *Mol. Imaging Biol.* **2018**, *20*, 902–918, doi:10.1007/s11307-018-1265-0.
9. Adamson, E.B.; Ludwig, K.D.; Mummy, D.G.; Fain, S.B. Magnetic resonance imaging with hyperpolarized agents: Methods and applications. *Phys. Med. Biol.* **2017**, *62*, R81–R123, doi:10.1088/1361-6560/aa6be8.
10. Ardenkjaer-Larsen, J.H.; Leach, A.M.; Clarke, N.; Urbahn, J.; Anderson, D.; Skloss, T.W. Dynamic nuclear polarization polarizer for sterile use intent. *NMR Biomed.* **2011**, *24*, 927–932, doi:10.1002/nbm.1682.
11. Ardenkjaer-Larsen, J.H. On the present and future of dissolution-DNP. *J. Magn. Reson.* **2016**, *264*, 3–12, doi:10.1016/j.jmr.2016.01.015.
12. Singh, J.; Suh, E.H.; Sharma, G.; Khemtong, C.; Sherry, A.D.; Kovacs, Z. Probing carbohydrate metabolism using hyperpolarized 13C-labeled molecules. *NMR Biomed.* **2019**, *32*, e4018, doi:10.1002/nbm.4018.
13. Wang, Z.J.; Ohliger, M.A.; Larson, P.E.Z.; Gordon, J.W.; Bok, R.A.; Slater, J.; Villanueva-Meyer, J.E.; Hess, C.P.; Kurhanewicz, J.; Vigneron, D.B. Hyperpolarized 13C MRI: State of the Art and Future Directions. *Radiology* **2019**, *291*, 273–284, doi:10.1148/radiol.2019182391.
14. Hoult, D.I.; Richards, R.E. The signal-to-noise ratio of the nuclear magnetic resonance experiment. 1976. *J. Magn. Reson.* **2011**, *213*, 329–343, doi:10.1016/j.jmr.2011.09.018.
15. Jin, J. *Electromagnetic Analysis and Design in Magnetic Resonance Imaging*; Routledge & CRC Press: Abingdon, UK, 1999.
16. Edelstein, W.A.; Glover, G.H.; Hardy, C.J.; Redington, R.W. The intrinsic signal-to-noise ratio in NMR imaging. *Magn. Reson. Med.* **1986**, *3*, 604–618, doi:10.1002/mrm.1910030413.
17. Hoult, D.I.; Lauterbur, P.C. The sensitivity of the zeugmatographic experiment involving human samples. *J. Magn. Reson.* **1979**, *34*, 425–433, doi:10.1016/0022-2364(79)90019-2.
18. Giovannetti, G.; Hartwig, V.; Frijia, F.; Menichetti, L.; Positano, V.; Ardenkjaer-Larsen, J.H.; Lionetti, V.; Aquaro, G.D.; De Marchi, D.; Flori, A.; et al. Hyperpolarized 13C MRS Cardiac Metabolism Studies in Pigs: Comparison Between Surface and Volume Radiofrequency Coils. *Appl. Magn. Reson.* **2012**, *42*, doi:10.1007/s00723-011-0307-4.
19. Yee, K.S. Numerical solution of initial boundary value problems involving Maxwell's equations in isotropic media. *IEEE Trans. Antennas Propag.* **1966**, 302–307, doi:10.1109/TAP.1966.1138693.
20. Amjad, A.; Kamondetdacha, R.; Kildishev, A.V.; Park, S.M.; Nyenhuis, J.A. Power deposition inside a phantom for testing of MRI heating. *IEEE Trans. Magn.* **2005**, *41*, 4185–4187, doi:10.1109/TMAG.2005.854840.
21. Chen, J.; Feng, Z.; Jin, J.-M. Numerical simulation of SAR and B_1 field inhomogeneity of shielded RF coils loaded with the human head. *IEEE Trans. Biomed. Eng.* **1998**, *45*, 650–659, doi:10.1109/10.668756.
22. Wang, Z.; Lin, J.C.; Mao, W.; Liu, W.; Smith, M.B.; Collins, C.M. SAR and temperature: Simulations and comparison to regulatory limits for MRI. *J. Magn. Reson. Imaging* **2007**, *26*, 437–441, doi:10.1002/jmri.20977.

23. Seo, J.H.; Heo, H.J.; Han, B.H.; Lee, S.Y. Comparison of Birdcage and Phase Array Coil Using FDTD for the B_1 Homogeneity in High Field MRI. In Proceedings of the 29th Annual International Conference of the IEEE Engineering in Medicine and Biology Society, Lyon, France, 23–26 August 2007; pp. 3902–3905, doi:10.1109/IEMBS.2007.4353186.

24. Sullivan, D.M.; Nadobny, J. FDTD simulation of RF coils for MRI. In Proceedings of the IEEE Antennas and Propagation Society International Symposium, North Charleston, SC, USA, 1–5 June 2009; pp. 1–4, doi:10.1109/APS.2009.5171798.

25. Hikage, T.; Kawamura, Y.; Nojima, T.; Cabot, E. Numerical assessment methodology for active implantable medical device EMI due to magnetic resonance wireless power transmission antenna. *Int. Symp. Electromagn. Compat. EMC Eur.* **2012**, 1–6, doi:10.1109/EMCEurope.2012.6396797.

26. Hurlston, S.E.; Brey, W.W.; Suddarth, S.A.; Johnson, G.A. A high-temperature superconducting Helmholtz probe for microscopy at 9.4 T. *Magn. Reson. Med.* **1999**, *41*, 1032–1038, doi:10.1002/(sici)1522-2594(199905)41:5.

27. Chen, C.N.; Hoult, D.I. *Biomedical Magnetic Resonance Technology*; Adam Hilger: Bristol, UK, 1989.

28. Belevitch, V. Lateral skin effect in a flat conductor. *Philips. Technol. Rev.* **1971**, *32*, 221–231.

29. Giovannetti, G.; Hartwig, V.; Landini, L.; Santarelli, M.F. Classical and lateral skin effect contributions estimation in strip MR coils. *Concepts Magn. Reson. Part B Magn. Reson. Eng.* **2012**, *41B*, 57–61, doi:10.1002/cmr.b.21210.

30. Giovannetti, G.; Viti, V.; liu, Y.; Yu, W.; Mittra, R.; Landini, L.; Benassi, A. An accurate simulator for magnetic resonance coil sensitivity estimation. *Concepts Magn. Reson. Part B Magn. Reson. Eng.* **2008**, *33B*, 209–215, doi:10.1002/cmr.b.20121.

31. Vaughan, J.T.; Griffiths, J.R. *RF Coils for MRI*; Wiley: Hoboken, NJ, USA, 2012.

32. Hayes, C.E.; Edelstein, W.A.; Schenck, J.F.; Mueller, O.M.; Eash, M. An efficient, highly homogeneous radiofrequency coil for whole-body NMR imaging at 1.5 T. *J. Magn. Reson.* **1985**, *63*, 622–628, doi:10.1016/0022-2364(85)90257-4.

33. Roemer, P.B.; Edelstein, W.A.; Hayes, C.E.; Souza, S.P.; Mueller, O.M. The NMR phased array. *Magn. Reson. Med.* **1990**, *16*, 192–225, doi:10.1002/mrm.1910160203.

34. Darrasse, L.; Ginefri, J.C. Perspectives with cryogenic RF probes in biomedical MRI. *Biochimie* **2003**, *85*, 915–937, doi:10.1016/j.biochi.2003.09.016.

35. Giovannetti, G.; Frijia, F.; Hartwig, V.; Menichetti, L.; De Marchi, D.; Positano, V.; Landini, L.; Lombardi, M.; Santarelli, M.F.; Ardenkjaer-Larsen, J.H. A novel method for coil efficiency estimation: Validation with a 13C birdcage. *Concepts Magn. Reson. Part B Magn. Reson. Eng.* **2012**, *41B*, 139–143, doi:10.1002/cmr.b.21223.

36. Freed, J.H.; Leniart, D.S.; Hyde, J.S. Theory of Saturation and Double Resonance Effects in ESR Spectra. III. rf Coherence and Line Shapes. *J. Chem. Phys.* **1967**, *47*, 2762–2773, doi:10.1063/1.1712295.

37. Giovannetti, G.; Frijia, F.; Hartwig, V.; Menichetti, L.; Ardenkjaer-Larsen, J.H.; De Marchi, D.; Positano, V.; Landini, L.; Lombardi, M.; Santarelli, M.F. Efficiency evaluation of a 13C Magnetic Resonance birdcage coil: Theory and comparison of four methods. *Measurement* **2013**, *46*, 2201–2205, doi:10.1016/j.measurement.

38. Keifer, P.A. 90° pulse width calibrations: How to read a pulse width array. *Concepts Magn. Reson.* **1999**, *11*, 165–180, doi:10.1002/(SICI)1099-0534(1999)11:3<165.

39. Hornak, J.P. *Encyclopedia of Imaging Science and Technology*; Wiley: Hoboken, NJ, USA, 2002.

40. Frijia, F.; Menichetti, L.; Lionetti, V.; Santarelli, M.F.; Ardenkjaer Larsen, J.H.; Giovannetti, G.; Positano, V.; De Marchi, D.; Aquaro, G.; Campan, M.; et al. Experimental approaches to cardiac imaging with hyperpolarized [1-13 c]pyruvate: A feasibility study in rats with a 3T clincal scanner. *J. Cardiovasc. Magn. Reson.* **2010**, *12*, 1–2.

41. Kohler, S.J.; Yen, Y.; Wolber, J.; Chen, A.P.; Albers, M.J.; Bok, R.; Zhang, V.; Tropp, J.; Nelson, S.; Vigneron, D.B.; et al. In vivo 13 carbon metabolic imaging at 3T with hyperpolarized 13C-1-pyruvate. *Magn. Reson. Med.* **2007**, *58*, 65–69, doi:10.1002/mrm.21253.

42. Durst, M.; Koellisch, U.; Frank, A.; Rancan, G.; Gringeri, C.V.; Karas, V.; Wiesinger, F.; Menzel, M.I.; Schwaiger, M.; Haase, A.; et al. Comparison of acquisition schemes for hyperpolarised 13C imaging. *NMR Biomed.* **2015**, *28*, 715–725, doi:10.1002/nbm.3301.

43. Xing, Y.; Reed, G.D.; Pauly, J.M.; Kerr, A.B.; Larson PE, Z. Optimal variable flip angle schemes for dynamic acquisition of exchanging hyperpolarized substrates. *J. Magn. Reson.* **2013**, *234*, 75–81, doi:10.1016/j.jmr.2013.06.003.

44. Day, S.E.; Kettunen, M.I.; Gallagher, F.A.; Hu, D.-E.; Lerche, M.; Wolber, J.; Golman, K.; Ardenkjaer-Larsen, J.H.; Brindle, K.M. Detecting tumor response to treatment using hyperpolarized 13C magnetic resonance imaging and spectroscopy. *Nat. Med.* **2007**, *13*, 1382–1387, doi:10.1038/nm1650.

45. Menichetti, L.; Frijia, F.; Flori, A.; Wiesinger, F.; Lionetti, V.; Giovannetti, G.; Aquaro, G.D.; Recchia, F.A. Assessment of real-time myocardial uptake and enzymatic conversion of hyperpolarized [1-13C]pyruvate in pigs using slice selective magnetic resonance spectroscopy. *Contrast Media Mol. Imaging* **2012**, *7*, 85–94, doi:10.1002/cmmi.480.

46. Mayer, D.; Yen, Y.-F.; Tropp, J.; Pfefferbaum, A.; Hurd, R.E.; Spielman, D.M. Application of subsecond spiral chemical shift imaging to real-time multislice metabolic imaging of the rat in vivo after injection of hyperpolarized 13C1-pyruvate. *Magn. Reson. Med.* **2009**, *62*, 557–564, doi:10.1002/mrm.22041.

47. Wiesinger, F.; Weidl, E.; Menzel, M.I.; Janich, M.A.; Khegai, O.; Glaser, S.J.; Haase, A.; Schwaiger, M.; Schulte, R.F. IDEAL spiral CSI for dynamic metabolic MR imaging of hyperpolarized [1-13C]pyruvate. *Magn. Reson. Med.* **2012**, *68*, 8–16, doi:10.1002/mrm.23212.

48. Schulte, R.F.; Sperl, J.I.; Weidl, E.; Menzel, M.I.; Janich, M.A.; Khegai, O.; Durst, M.; Ardenkjaer-Larsen, J.H.; Glaser, S.J.; Haase, A.; et al. Saturation-recovery metabolic-exchange rate imaging with hyperpolarized [1-13C] pyruvate using spectral-spatial excitation. *Magn. Reson. Med.* **2013**, *69*, 1209–1216, doi:10.1002/mrm.24353.

49. Flori, A.; Frijia, F.; Lionetti, V.; Ardenkjaer-Larsen, J.H.; Positano, V.; Giovannetti, G.; Schulte, R.F.; Wiesinger, F.; Recchia, F.A.; Landini, L.; et al. DNP Methods for Cardiac Metabolic Imaging with Hyperpolarized [1-13C]pyruvate Large Dose Injection in Pigs. *Appl. Magn. Reson.* **2012**, *43*, 299–310, doi:10.1007/s00723-012-0350-9.

50. Chen, A.P.; Albers, M.J.; Cunningham, C.H.; Kohler, S.J.; Yen, Y.-F.; Hurd, R.E.; Tropp, J.; Bok, R.; Pauly, J.M.; Nelson, S.J.; et al. Hyperpolarized C-13 spectroscopic imaging of the TRAMP mouse at 3T-initial experience. *Magn. Reson. Med.* **2007**, *58*, 1099–1106, doi:10.1002/mrm.21256.

51. Albers, M.J.; Bok, R.; Chen, A.P.; Cunningham, C.H.; Zierhut, M.L.; Zhang, V.Y.; Kohler, S.J.; Tropp, J.; Hurd, R.E.; Yen, Y.-F.; et al. Hyperpolarized 13C lactate, pyruvate, and alanine: Noninvasive biomarkers for prostate cancer detection and grading. *Cancer Res.* **2008**, *68*, 8607–8615, doi:10.1158/0008-5472.CAN-08-0749.

52. Larson, P.E.Z.; Hu, S.; Lustig, M.; Kerr, A.B.; Nelson, S.J.; Kurhanewicz, J.; Pauly, J.M.; Vigneron, D.B. Fast dynamic 3D MR spectroscopic imaging with compressed sensing and multiband excitation pulses for hyperpolarized 13C studies. *Magn. Reson. Med.* **2011**, *65*, 610–619, doi:10.1002/mrm.22650.

53. Hu, S.; Lustig, M.; Balakrishnan, A.; Larson, P.E.Z.; Bok, R.; Kurhanewicz, J.; Nelson, S.J.; Goga, A.; Pauly, J.M.; Vigneron, D.B. 3D compressed sensing for highly accelerated hyperpolarized (13)C MRSI with in vivo applications to transgenic mouse models of cancer. *Magn. Reson. Med.* **2010**, *63*, 312–321, doi:10.1002/mrm.22233.

54. Arunachalam, A.; Whitt, D.; Fish, K.; Giaquinto, R.; Piel, J.; Watkins, R.; Hancu, I. Accelerated spectroscopic imaging of hyperpolarized C-13 pyruvate using SENSE parallel imaging. *NMR Biomed.* **2009**, *22*, 867–873, doi:10.1002/nbm.1401.

55. Ohliger, M.A.; Larson, P.E.Z.; Bok, R.A.; Shin, P.; Hu, S.; Tropp, J.; Robb, F.; Carvajal, L.; Nelson, S.J.; Kurhanewicz, J.; et al. Combined parallel and partial fourier MR reconstruction for accelerated 8-channel hyperpolarized carbon-13 in vivo magnetic resonance Spectroscopic imaging (MRSI). *J. Magn. Reson. Imaging* **2013**, *38*, 701–713, doi:10.1002/jmri.23989.

56. Leupold, J.; Månsson, S.; Petersson, J.S.; Hennig, J.; Wieben, O. Fast multiecho balanced SSFP metabolite mapping of (1)H and hyperpolarized (13)C compounds. *Magn. Reson. Mater. Phys. Biol. Med.* **2009**, *22*, 251–256, doi:10.1007/s10334-009-0169-z.

57. Månsson, S.; Petersson, J.S.; Scheffler, K. Fast metabolite mapping in the pig heart after injection of hyperpolarized 13C-pyruvate with low-flip angle balanced steady-state free precession imaging. *Magn. Reson. Med.* **2012**, *68*, 1894–1899, doi:10.1002/mrm.24183.

58. Topping, G.J.; Hundshammer, C.; Nagel, L.; Grashei, M.; Aigner, M.; Skinner, J.G.; Schulte, R.F.; Schilling, F. Acquisition strategies for spatially resolved magnetic resonance detection of hyperpolarized nuclei. *Magn. Reson. Mater. Phys. Biol. Med.* **2020**, *33*, 221–256, doi:10.1007/s10334-019-00807-6.

59. Mispelter, J.; Lupu, M.; Briguet, A. *NMR Probeheads for Biophysical and Biomedical Experiments: Theoretical Principles and Practical Guidelines*, 2nd ed.; Imperial College Press: London, UK, 2015.

60. Giovannetti, G.; Frijia, F.; Menichetti, L.; Milanesi, M.; Ardenkjaer-Larsen, J.H.; De Marchi, D.; Hartwig, V.; Positano, V.; Landini, L.; Lombardi, M.; et al. Hyperpolarized 13C MRS surface coil: Design and signal-to-noise ratio estimation. *Med. Phys.* **2010**, *37*, 5361–5369, doi:10.1118/1.3491437.

61. Taylor, H.C.; Burl, M.; Hand, J.W. Experimental verification of numerically predicted electric field distributions produced by a radiofrequency coil. *Phys. Med. Biol.* **1997**, *42*, 1395–1402, doi:10.1088/0031-9155/42/7/012.

62. Vullo, T.; Zipagan, R.T.; Pascone, R.; Whalen, J.P.; Cahill, P.T. Experimental design and fabrication of birdcage resonators for magnetic resonance imaging. *Magn. Reson. Med.* **1992**, *24*, 243–252, doi:10.1002/mrm.1910240206.

63. Pascone, R.J.; Garcia, B.J.; Fitzgerald, T.M.; Vullo, T.; Zipagan, R.; Cahill, P.T. Generalized electrical analysis of low-pass and high-pass birdcage resonators. *Magn. Reson. Imaging* **1991**, *9*, 395–408, doi:10.1016/0730-725x(91)90428-o.

64. Giovannetti, G.; Frijia, F.; Hartwig, V.; Menichetti, L.; Positano, V.; Ardenkjaer-Larsen, J.H.; Lionetti, V.; Aquaro, G.D.; De Marchi, D.; Schulte, R.F.; et al. Transmit-Only/Receive-Only Radiofrequency System for Hyperpolarized 13C MRS Cardiac Metabolism Studies in Pigs. *Appl. Magn. Reson.* **2013**, *44*, 1125–1138, doi:10.1007/s00723-013-0477-3.

65. Giovannetti, G.; Frijia, F.; Hartwig, V.; Attanasio, S.; Menichetti, L.; Vanello, N.; Positano, V.; Ardenkjaer-Larsen, J.H.; Lionetti, V.; Aquaro, G.D.; et al. Design of a quadrature surface coil for hyperpolarized 13C MRS cardiac metabolism studies in pigs. *Concepts Magn. Reson. Part B Magn. Reson. Eng.* **2013**, *43*, 69–77, doi:10.1002/cmr.b.21235.

66. Giovannetti, G.; Frijia, F.; Attanasio, S.; Menichetti, L.; Hartwig, V.; Vanello, N.; Ardenkjaer-Larsen, J.H.; De Marchi, D.; Positano, V.; Schulte, R.; et al. Magnetic resonance butterfly coils: Design and application for hyperpolarized 13C studies. *Measurement* **2013**, *46*, 3282–3290, doi:10.1016/j.measurement.2013.06.031.

67. Giovannetti, G.; Hartwig, V.; Frijia, F.; Menichetti, L.; Positano, V.; Ardenkjær-Larsen, J.H.; Landini, L.; Lombardi, M.; Santarelli, M.F. Simulation and comparison of coils for Hyperpolarized 13C MRS cardiac metabolism studies in pigs. *Measurement* **2015**, *60*, 78–84, doi:10.1016/j.measurement.2014.09.065.

68. Frijia, F.; Santarelli, M.F.; Koellisch, U.; Giovannetti, G.; Lanz, T.; Flori, A.; Durst, M.; Aquaro, G.D.; Schulte, R.F.; De Marchi, D.; et al. 16-Channel Surface Coil for 13C-Hyperpolarized Spectroscopic Imaging of Cardiac Metabolism in Pig Heart. *J. Med. Biol. Eng.* **2016**, *36*, 53–61, doi:10.1007/s40846-016-0113-4.

69. Giovannetti, G.; Flori, A.; Marsigli, F.; De Marchi, D.; Frijia, F.; Giannoni, M.; Kusmic, C.; Positano, V.; Aquaro, G.D.; Menichetti, L. A radiofrequency system for in vivo hyperpolarized 13 C MRS experiments in mice with a 3T MRI clinical scanner. *Scanning* **2016**, *38*, 710–719, doi:10.1002/sca.21319.

70. Yang, Z.; Liu, W.; Basham, E. Inductor modeling in wireless links for implantable electronics. *Appl. Supercond. Conf.* **2007**, *43*, 3851–3860, doi:10.1109/TMAG.2007.904189.

71. Minard, K.R.; Wind, R.A. Solenoidal microcoil design—Part II: Optimizing winding parameters for maximum signal-to-noise performance. *Concepts Magn. Reson.* **2001**, *13*, 190–210, doi:10.1002/cmr.1008.

72. Meyerspeer, M.; Serés Roig, E.; Gruetter, R.; Magill, A.W. An improved trap design for decoupling multinuclear RF coils. *Magn. Reson. Med.* **2014**, *72*, 584–590, doi:10.1002/mrm.24931.

73. Niendorf, T.; Graessl, A.; Thalhammer, C.; Dieringer, M.A.; Kraus, O.; Santoro, D.; Fuchs, K.; Hezel, F.; Waiczies, S.; Ittermann, B.; et al. Progress and promises of human cardiac magnetic resonance at ultrahigh fields: A physics perspective. *J. Magn. Reson.* **2013**, *229*, 208–222, doi:10.1016/j.jmr.2012.11.015.

74. Aquaro, G.D.; Frijia, F.; Positano, V.; Menichetti, L.; Santarelli, M.F.; Ardenkjaer-Larsen, J.H.; Wiesinger, F.; Lionetti, V.; Romano, S.L.; Bianchi, G.; et al. 3D CMR mapping of metabolism by hyperpolarized 13C-pyruvate in ischemia-reperfusion. *JACC Cardiovasc. Imaging* **2013**, *6*, 743–744, doi:10.1016/j.jcmg.2012.11.023.

75. Flori, A.; Liserani, M.; Frijia, F.; Giovannetti, G.; Lionetti, V.; Casieri, V.; Positano, V.; Aquaro, G.D.; Recchia, F.A.; Santarelli, M.F.; et al. Real-time cardiac metabolism assessed with hyperpolarized [1-(13)C]acetate in a large-animal model. *Contrast Media Mol. Imaging* **2015**, *10*, 194–202, doi:10.1002/cmmi.1618.